A Synergistic GPR Approach of Back Projection Algorithm and Full-Wave Inversion for Reconstruction in Unknown Multilayered Environments

Zihan Xu, Hongxu Li, Xinfei Jin, Fulin Su, Guodong Xu, and Sébastien Lambot, *Member, IEEE*

***Abstract*— Ground-penetrating radar (GPR) has become indispensable for subsurface reconstruction, especially in complex, multilayered infrastructure environments. Efficient and accurate estimation of permittivity and layer thickness, crucial for understanding these scenes, presents significant challenges. This article explores the integration and interaction between the back projection (BP) algorithm and full-wave inversion (FWI) to optimize reconstruction outcomes. We propose a ray-based refraction method and a high-order moment (HOM)-oriented local BP estimation, each aimed at improving efficiency from the critical perspectives of "delay" and "summation" in the BP algorithm, respectively, with a focus on the target layer. Crucially, the BP estimation results provide a reliable initial model for FWI, reducing the risk of local minima and decreasing the iteration count for more precise parameter estimation. FWI also compensates for the BP algorithm's limitations in estimating parameters in nontarget layers. Furthermore, full-wave modeling (FWM) mitigates antenna effects prior to parameter estimation, thereby enhancing accuracy. During reconstruction, the BP algorithm primarily generates target imaging, while FWI provides detailed information about layer interfaces. This synergistic approach leverages the complementary strengths of both algorithms: the BP algorithm captures spatial information depicted by the targets observed in B-scans, while FWI incorporates detailed electromagnetic wave propagation along layer interfaces presented in A-scans via radar equations. Experiments systematically analyze the accuracy and effectiveness of the proposed approach using ideal simulation models, sandbox laboratory data, and road data from the Belgian Road Research Centre (BRRC) facilities. This comprehensive evaluation underscores the approach's substantial potential in advanced geophysical surveys and environmental research.**

***Index Terms*— Back projection (BP), estimation, full-wave modeling (FWM) and full-wave inversion (FWI), ground-penetrating radar (GPR), layered media.**

I. INTRODUCTION

GROUND-PENETRATING radar (GPR) has revolutionized the way researchers and practitioners visualize and analyze the subsurface realm. It employs high-frequency electromagnetic waves to probe beneath the surface [1], revealing hidden structures and materials. As a noninvasive geophysical method, this technology is critical for managing infrastructure, including railroads, dams, bridges, airfields, and inland navigation facilities [2], [3]. These infrastructures often consist of complex multilayered structures and contain materials, such as buried pipes and steel bars [4], [5]. Moreover, unknown conditions like voids and leaks may occur as facilities age or due to construction impacts [6]. In addition, the foundation environments are influenced by dynamic factors, for instance, water content [7]. Although GPR holds broad prospects, significant challenges remain in reconstructing scenes and further accurately interpreting underground features in unknown multilayered environments.

Given the frequent presence of point targets, such as pipelines, cavities, and rocks [8], [9], [10] in subterranean environments, numerous reconstruction algorithms have been designed based on the hyperbolic echoes generated by these point targets. These reconstruction algorithms, represented by so-called migration techniques, focus hyperbolas to their vertices and accurately pinpoint their positions [11], [12]. The migration techniques are notably sensitive to the permittivity of the medium, which impacts the focusing of hyperbolic curves. Exploiting this relationship, the focus criterion is used to estimate the soil permittivity, thus achieving precise reconstruction of unknown environments [13]. Weibull and Arntsen [14] applied an automatic method to estimate the background velocities using reverse-time migration (RTM) algorithm, based on combination of differential semblance and similarity-index. Nguyen et al. [15] combined automatic/semiautomatic strategies and applied the Kirchhoff migration to common offset GPR data. Lv and Zhang [16] proposed a high-resolution permittivity estimation

Received 19 July 2024; revised 23 September 2024, 23 October 2024, and 5 November 2024; accepted 12 November 2024. Date of publication 18 November 2024; date of current version 2 December 2024. This work was supported in part by China Scholarship Council (CSC), China; in part by the Fonds de la Recherche Scientifique (FNRS), Belgium; in part by the Belgian Road Research Centre (BRRC), Belgium; in part by Harbin Institute of Technology (HIT), China; and in part by the Université catholique de Louvain (UCLouvain), Belgium. *(Corresponding author: Fulin Su.)*

Zihan Xu is with the Earth and Life Institute, Université catholique de Louvain, 1348 Ottignies-Louvain-la-Neuve, Belgium, and also with Harbin Institute of Technology, Harbin 150001, China (e-mail: zihan.xu@stu.hit.edu.cn).

Hongxu Li, Xinfei Jin, Fulin Su, and Guodong Xu are with Harbin Institute of Technology, Harbin 150001, China (e-mail: 20B905041@stu.hit.edu.cn; 19B905044@stu.hit.edu.cn; franklin_su@hit.edu.cn; xuguodong@hit.edu.cn).

Sébastien Lambot is with the Earth and Life Institute, Université catholique de Louvain, 1348 Ottignies-Louvain-la-Neuve, Belgium.

Digital Object Identifier 10.1109/TGRS.2024.3500588

by migration with isolated hyperbolic diffractions. However, these methods are based on homogeneous medium models and are unable to effectively handle complex environments. In addition, they require lengthy iteration times. Jung et al. [17] introduced the Stolt migration algorithm into multilayered media. The group also extended Stolt migration to oblique layer scenarios and compared it with the RTM algorithm, highlighting its efficiency advantages [18], [19]. However, the Stolt migration is dependent on the target depth, which limits its ability to detect deep targets. Compared with the Stolt migration algorithm, the back projection (BP) algorithm offers significant advantages in terms of depth independence. Xu et al. [20] introduced the BP algorithm into the parameter estimation and reconstruction of a homogeneous medium, conducting a comparative analysis with the Stolt migration algorithm to validate its unique potential in the reconstruction of unknown environments. However, the reconstruction efficiency of the BP algorithm in unknown multilayered media remains a challenge. This is primarily evident in the "delay" solution and "summation" process required for each imaging point. While some approximation algorithms aim to enhance the efficiency of the BP algorithm, a substantial number of iterative processes are still required [21] or are only used in two-layer scenarios [22]. In brief, while migration techniques have demonstrated good results in controlled settings, they remain limited when applied to the complex environments and requirements of actual engineering. Specifically, these techniques face challenges in dealing with complex, multilayered media. The BP algorithm, on the other hand, shows significant potential in addressing these challenges. However, its current implementation suffers from inefficiencies, particularly in such demanding applications. Therefore, our work focuses on enhancing the reconstruction efficiency of the BP algorithm, specifically for use in unknown, multilayered environments, to overcome the limitations of existing methods.

Another noteworthy consideration is that the aforementioned hyperbola-based permittivity reconstruction techniques heavily rely on point targets within the environment. However, in practical infrastructure detection scenarios, buried objects such as pipelines are often absent in shallow media [23]. Solely depending on hyperbolas renders the reconstruction process lacking in robustness and unsuitable for real-world engineering detection applications. Furthermore, the antenna effects are inherently present in echoes during the detection process, often manifesting as horizontal clutter, which significantly impacts the determination of layer interfaces [24] and the judgment of focus criteria, thereby rendering reconstruction methods ineffective. Considering these two aspects, full-wave modeling (FWM) and full-wave inversion (FWI) based on Green's functions can effectively complement this deficiency. The FWM proposed by Lambot et al. [25] take into account both the multiple reflections within the antenna and between the antenna and the medium for far-field conditions. This enables the preprocessing and inversion of GPR data by accounting for this significant clutter, greatly enhancing the accuracy and robustness of the inversion. FWI has shown considerable potential across various applications, including soil moisture measurement [26], trunk monitoring [27], and utility detection [28]. Furthermore, the technique can be adapted for the development of GPR in diverse configurations, including bistatic setups [29]. However, as is common in electromagnetic inverse problems, the process of FWI is highly nonlinear, and the objective function to minimize usually displays oscillatory behavior characterized by numerous local minima. Utilizing the traditional Nelder–Mead simplex (NMS) algorithm [30] for minimizing the objective function relies heavily on an excellent initial model, which is impractical for GPR detection in unknown media. The global optimization by multilevel coordinate search (MCS), when combined with the classical NMS algorithm [31], [32], can iteratively approach the global minimum, though this process is time-consuming. A look-up table approach enables near-real-time inversion; however, it necessitates presetting parameters, calculating, and storing forward Green's functions. In unfamiliar scenarios, this approach often entails a significant workload and substantial storage requirements [33]. Leveraging multifrequency data can aid in simplifying the objective function topography and related optimization process, but this requires additional information and possibly a combination with the convolutional neural network [34].

To address the above issues, this article proposes a synergistic GPR approach integrating the BP algorithm and FWI for reconstructing unknown layered environments, especially in the infrastructure detection. To mitigate the time-consuming nature of the BP algorithm during iterative parameter estimation, we introduce a ray-based refraction method, which circumvents the iterative approximation of refraction point positions in the BP algorithm's "delay" solution by directly estimating them using a system of linear equations. Subsequently, a high-order moment (HOM)-oriented local BP estimation method is proposed to significantly reduce redundancy in its "summation" process. In practical detection scenarios, we utilize FWM to eliminate antenna effects and enhance the robustness of layer interface detection. The integration and interaction between the BP algorithm and the FWI algorithm are evident throughout the estimation and reconstruction process. The BP estimation relies on the target scene, where point targets are typically absent in the shallow layers of road surfaces, making FWI a valuable complement. In deeper scenes, the construction of the FWI significantly increases computation time due to the signal time, especially when coupled with MCS and NMS, leading to reduced efficiency. At this juncture, the BP algorithm furnishes a robust initial model, enabling FWI to conduct efficient estimation employing fast local optimization algorithms exclusively. During the reconstruction process, the BP algorithm adeptly focuses on hyperbolas while allocating comparatively less attention to layer interfaces. Particularly in BP imaging, to enhance target clarity, horizontal interface responses are typically removed, leading to a perception of interface fragmentation. Here, FWI's precise inversion of layer interfaces serves as a perfect complementary measure. The collaborative synergy between the BP algorithm and FWI algorithm jointly promotes the accurate reconstruction of multilayered environments. This article is equipped with a comprehensive set of experiments, ranging from simulated data, and sandbox experiments, to Belgian road exploration. It progressively examines the effectiveness of the proposed method from three perspectives: the performance of the BP algorithm in ideal environments, the impact of antenna effects, and strategies for practical detection. This comprehensive analysis thoroughly evaluates the efficacy of the proposed method in both theoretical derivation and engineering applications.

II. BP Algorithm in Unknown Multilayered Environments

In a multilayered environment with prior information, the BP algorithm can be conceptualized as a "delay–summation" process, as illustrated in Fig. 1. The model is composed of N layers of media, each characterized by distinct electromagnetic properties. The nth layer is defined by relative permittivity ε_n and thickness h_n. In the model for the BP algorithm, we account for the magnetic permeability of free space, which is appropriate for the majority of detection environments. In addition, the conductivity in the model is set to 0, a critical assumption since it does not reflect real-world conditions except in very dry, clay-free soils [35]. However, given that the BP algorithm relies on travel times rather than amplitudes, this assumption remains valid. In this setup, a mobile platform, equipped with a transceiving antenna, traverses along the detection line. The antenna periodically transmits pulses and receives echoes that result from permittivity discontinuities within the layers. The round-trip delay, denoted by $t_{A_k P}$, spans from the antenna position $A(x_k, 0)$ to the imaging point P. With K repeated operations of the antenna along the detection line, the imaging result S_P of the BP algorithm for the imaging point P can be expressed as follows:

$$S_P = \sum_{k=1}^{K} s_k\left(t_{A_k P}\right) \tag{1}$$

where s_k represents the time-domain signal collected by the antenna at the position $(x_k, 0)$ and K represents the number of antennas illuminating the imaging point P.

While the mathematical model of the BP algorithm is straightforward and lucid, resolving the key parameter delay $t_{A_k P}$ poses a significant challenge. As shown in Fig. 1, a connection exists between each pair of adjacent media layers, as dictated by Snell's Law

$$\frac{(x_{n-1} - x_{n-2})^2}{(x_{n-1} - x_{n-2})^2 + h_{n-1}^2} \cdot \frac{\left(x_p - x_{n-1}\right)^2 + h_p^2}{\left(x_p - x_{n-1}\right)^2} = \frac{\varepsilon_n}{\varepsilon_{n-1}}. \tag{2}$$

It is evident that there exists a fourth-order relationship, as expressed in (2), between any two adjacent layers of media. Furthermore, similar connections exist among the N layers as well

$$\sqrt{\varepsilon_1}\sin\theta_1 = \cdots = \sqrt{\varepsilon_n}\sin\theta_n = \cdots = \sqrt{\varepsilon_N}\sin\theta_N. \tag{3}$$

Equation (3) highlights the significant role of the permittivity in the BP algorithm. Fig. 2 details this influence by using the hyperbolic responses of a point target in a homogeneous medium as an example. Fig. 2(a) depicts a detection scenario

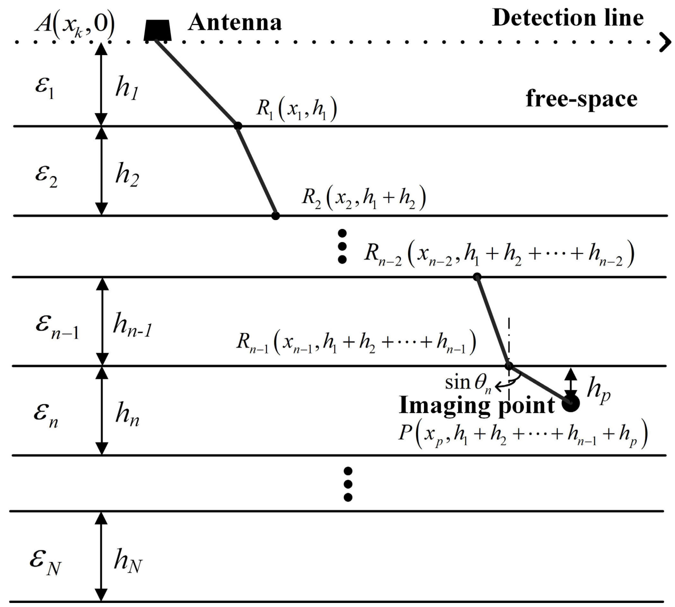

Fig. 1. BP algorithm in multilayered environments. The antenna moves horizontally in free space. The relative permittivity and thickness of the nth layer are ε_n and h_n, respectively. The imaging point is located in the nth layer, with a depth of h_p from the upper interface. The path of the electromagnetic wave is shown as a black bold line, with the refraction angle at the nth layer being θ_n.

within a homogeneous medium spanning 1 m, characterized by a relative permittivity of 5, with a point target buried at a depth of 0.4 m, which was simulated using the open-source software gprMax [36]. Fig. 2(b) shows the results of removing direct waves from the B-scan response simulated by the renowned open-source software, gprMax. The movement of the source and the point target produces a hyperbolic-shaped echo. Subsequently, Fig. 2(c) showcases the BP imaging results with the true relative permittivity of the model. The hyperbola is clearly focused, pinpointing the target's depth at 0.4 m. Conversely, when the input relative permittivity deviates from the true value, as illustrated in Fig. 2(d) (less) and (e) (greater), the BP algorithm fails to focus and yields upward and downward curves, respectively.

In a known multilayered environment, the time-consuming calculation of Fermat's principle is necessary. Furthermore, in an environment lacking prior knowledge, a series of permittivities must be inputted into the BP algorithm to iteratively perform imaging layer by layer. The estimation of permittivity and thickness of each layer is contingent upon the focus metric achieved.

However, utilizing the BP algorithm for permittivity estimation introduces two notable drawbacks. First, the estimation process necessitates inputting the test permittivity to iteratively image the scene, resulting in redundancy and time-consuming computations. This encompasses two time-consuming aspects: one involves the time delay, namely, the calculation of the refraction point, and the other pertains to the computational redundancy associated with imaging the entire scene. Second, clutter in the real scene may obscure contributions from the target hyperbola, leading to a degradation in imaging quality. Therefore, the careful selection

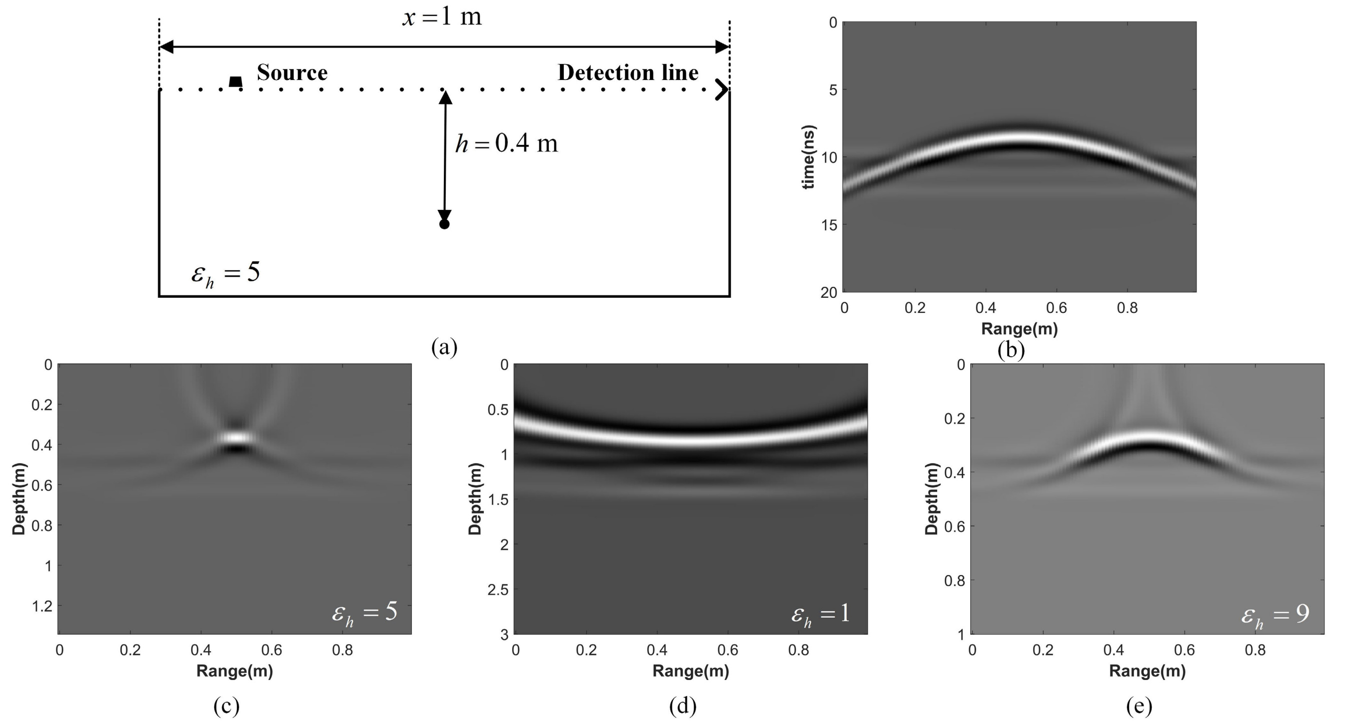

Fig. 2. Influences of different permittivities on the BP algorithm. (a) and (b) Homogeneous medium model and its preprocessed B-scan echoes, respectively. (c)–(e) Results of the BP algorithm when the input permittivity are equal to, less than, and greater than the true value.

of the hyperbola is crucial for achieving optimal results. In Sections II-A and II-B, we introduce two solutions to overcome these limitations.

A. Ray-Based Refraction Method in Multilayered Media

The pivotal task in determining the time delay $t_{A_k P}$ entails computing the positions of the refraction points at the layer interfaces. Nevertheless, as indicated by (2), when dealing with two layers, an iterative approximation becomes necessary for determining the refraction point. With the expansion to N layers, the computational complexity experiences a substantial surge, resulting in a marked increase in the calculation.

Johansson and Mast [37] succinctly encapsulated the computation of refraction points in a two-layer model within a linear expression, namely,

$$x_{n-1} = x_p + \sqrt{\frac{\varepsilon_{n-1}}{\varepsilon_n}} \frac{(x_{n-2} - x_p) h_p}{h_p + h_{n-1}}. \tag{4}$$

However, this linear expression only applies to a two-layer environment, and the permittivity of the lower layer surpasses or equals that of the upper layer ($\varepsilon_n \geq \varepsilon_{n-1}$).

In this article, we first consider the other case where the permittivity of the lower layer exceeds that of the upper layer ($\varepsilon_n < \varepsilon_{n-1}$). It refines the entire refraction point estimation process, laying the foundation for handling various situations during the propagation of electromagnetic waves in the multilayered media.

Fig. 3 focuses on two adjacent layers of Fig. 1. The line connecting the antenna position R_{n-2} and the target P intersects at the point M on the media boundary. Derived from the geometric relationship, a foundational point M is determined

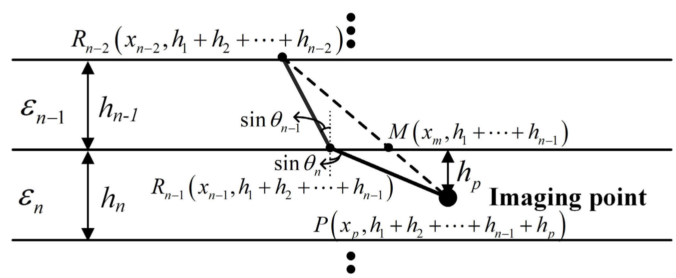

Fig. 3. Ray-based refraction method in two-layer model ($\varepsilon_n < \varepsilon_{n-1}$).

$$x_m = x_{n-2} - \frac{h_{n-1}}{h_{n-1} + h_p}(x_{n-2} - x_p). \tag{5}$$

Examine the following extreme cases.

1) In case $\varepsilon_n = \varepsilon_{n-1}$ ($\sin\theta_{n-1}/\sin\theta_n$=1), the ray will undergo no refraction. Therefore, the horizontal position of the refraction point x_p aligns with the point x_m, denoted by $x_{n-1} = x_m$.
2) When $\varepsilon_{n-1} \gg \varepsilon_n$, in compliance with Snell's law, where $\sin\theta_{n-1}/\sin\theta_n \to 0$, then the refraction point R_{n-1} coincides with the point R_{n-2}, i.e., $x_{n-1} = x_{n-2}$.
3) When the value of $\sin\theta_{n-1}/\sin\theta_n$ falls between 0 and 1, the point R_{n-1} lies within the range defined by R_{n-2} and M. Consequently, we utilize the neighboring permittivity to refine the position of point M in order to estimate the refraction point R_{n-1}

$$x_{n-1} = x_{n-2} - \sqrt{\frac{\varepsilon_n}{\varepsilon_{n-1}}} \frac{h_{n-1}}{h_{n-1} + h_p}(x_m - x_{n-2}). \tag{6}$$

Rearrange (6) to derive the linear estimated refraction point in the case of $\varepsilon_n < \varepsilon_{n-1}$

$$x_{n-1} = x_{n-2} + \sqrt{\frac{\varepsilon_n}{\varepsilon_{n-1}}}\frac{(x_p - x_{n-2})h_{n-1}}{h_p + h_{n-1}}. \tag{7}$$

The linear expression (7) showcases the inherent beauty of mathematical symmetry in conjunction with the Johansson's algorithm. Taking a deeper dive, let us delve into the profound connection between these two aspects and extend the exploration to N layers of media.

First, the relationship between the permittivity of the two adjacent layers $(n-1)$th and nth is consistently expressed as follows, where their ratio of the permittivities is redefined as $\widetilde{\varepsilon}_n$:

$$\sqrt{\widetilde{\varepsilon}_n} = \begin{cases} \sqrt{\dfrac{\varepsilon_{n-1}}{\varepsilon_n}}, & \dfrac{\varepsilon_n}{\varepsilon_{n-1}} \geq 1 \\ \sqrt{\dfrac{\varepsilon_n}{\varepsilon_{n-1}}}, & \dfrac{\varepsilon_n}{\varepsilon_{n-1}} < 1. \end{cases} \tag{8}$$

For the sake of clarity in subsequent discussions, this article henceforth denotes the coordinates of the imaging point P as $(x_n, h_1+\cdots+h_n)$. Furthermore, let $H_n = ((\widetilde{\varepsilon}_n)^{1/2}/h_n + h_{n-1})$, the estimated position of the refraction point at the interface of the $(n-1)$th and nth layers can be expressed as follows:

$$x_{n-1} = \begin{cases} (1 - H_n h_n)x_n + H_n h_n x_{n-2}, & \dfrac{\varepsilon_n}{\varepsilon_{n-1}} \geq 1 \\ H_n h_{n-1} x_n + (1 - H_n h_{n-1})x_{n-2}, & \dfrac{\varepsilon_n}{\varepsilon_{n-1}} < 1. \end{cases} \tag{9}$$

At this juncture, the estimation of Johansson's and our proposed method can be seamlessly integrated into a linear expression as shown in the following equation:

$$x_{n-1} = A_n x_n + B_n x_{n-2} \tag{10}$$

where

$$A_n = \begin{cases} 1 - H_n h_n, & \dfrac{\varepsilon_n}{\varepsilon_{n-1}} \geq 1 \\ H_n h_{n-1}, & \dfrac{\varepsilon_n}{\varepsilon_{n-1}} < 1 \end{cases} \tag{11}$$

$$B_n = \begin{cases} H_n h_n, & \dfrac{\varepsilon_n}{\varepsilon_{n-1}} \geq 1 \\ 1 - H_n h_{n-1}, & \dfrac{\varepsilon_n}{\varepsilon_{n-1}} < 1. \end{cases} \tag{12}$$

If antenna A reaches the imaging point P on the nth layer, and the horizontal coordinates of the refraction point through which the electromagnetic waves pass to be designated as $x_1, x_2, \ldots,$ and x_{n-1}, respectively, their relationship can be formulated as follows:

$$\begin{aligned} x_1 &= A_2 x_2 + B_2 x_0 \\ x_2 &= A_3 x_3 + B_3 x_1 \\ x_3 &= A_4 x_4 + B_4 x_2 \\ &\cdots \\ x_{n-2} &= A_{n-1} x_{n-1} + B_{n-1} x_{n-3} \\ x_{n-1} &= A_n x_n + B_n x_{n-2}. \end{aligned} \tag{13}$$

Therefore, our ray-based refraction method in multilayered media results in a concise tridiagonal linear system of equations as (14), as shown at the bottom of the next page. The tridiagonal linear equations can be efficiently solved using classical methods like the Gaussian elimination method, eliminating the need for iterative calculations and significantly reducing the overall computation time.

B. HOM-Oriented Local BP Estimation Method

In the process of parameter estimation based on the BP algorithm, we found that iterating imaging over the entire scene is not advisable. This is because clutter adversely affects imaging quality and focus metrics (such as image entropy), thus influencing the estimation results. In addition, targets are sparse relative to the entire scene, and computing regions without targets introduces significant computational redundancy. The challenge lies in determining which hyperbola to choose for parameter estimation. Therefore, we introduce an HOM-oriented local BP estimation method in multilayered media. Indeed, HOMs encompass various orders; here, we specifically focus on the fourth order. This is because of its profound mathematical significance, which aligns with the current context.

In probability theory and mathematical statistics, the fourth-order moment of variable $(x_1, x_2, \ldots, x_k)$ can be expressed as follows:

$$\text{HOM} = \frac{\sum_{i=1}^{k}(x_i - \mu)^4}{(k-1)\sigma^4} \tag{15}$$

where μ and σ are the mean $\mu = (1/k)\sum_{i=1}^{k} x_i$ and the standard deviation $\sigma = [(1/k-1)\sum_{i=1}^{k}(x_i - \mu)^2]^{1/2}$, respectively.

The fourth-order moment HOM can effectively characterize the distribution of data, with its physical interpretation representing kurtosis. Higher kurtosis is attributed to infrequent extreme deviations in the data, contrasting with frequent small deviations. Hence, the HOM proves valuable in delineating the concentrated distribution of data. Examine the real GPR data, as depicted in Fig. 4. It comprises three primary components: the targets, clutter, and background. Owing to the sparse distribution of targets, the received target responses exhibit a pronounced bias from the background. The contrast between the target and the background reaches its maximum at the vertex of the hyperbola due to the lowest attenuation of electromagnetic waves for that point. Therefore, when the automatic detection algorithm identifies the position of each hyperbola vertex, we can establish an $D \times N$ window centered on the vertex position and compute the fourth-order moment within each hyperbola vertex window. The HOM here can be expressed as (16). Higher kurtosis indicates a more concentrated distribution of data. Therefore, we can precisely extract the hyperbola vertex situated in regions characterized by a high signal-to-clutter ratio by selecting the maximum value of HOM

$$\text{HOM} = \frac{\sum_{m=1}^{D}\sum_{n=1}^{N}(s(x_m, t_n) - \mu)^4}{(DN-1)\sigma^4} \tag{16}$$

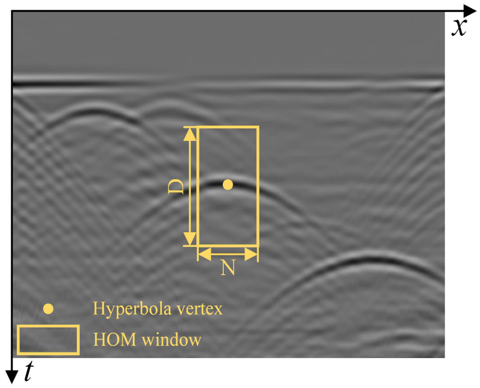

Fig. 4. HOM-oriented hyperbola extraction. The dot indicates the extracted hyperbola vertex, while the box delineates the local region utilized for BP imaging.

where

$$\begin{cases} \mu = \dfrac{1}{DN}\displaystyle\sum_{m=1}^{D}\sum_{n=1}^{N} s(x_m, t_n) \\ \sigma = \left[\dfrac{1}{DN-1}\displaystyle\sum_{m=1}^{D}\sum_{n=1}^{N}\left(s(x_m, t_n) - \mu\right)^2\right]^{1/2}. \end{cases} \tag{17}$$

It can be observed from Fig. 3 that deviations from the true permittivity lead to shifts in the hyperbola's imaging results, either upward or downward. Consequently, when defining the two parameters, D and N, the recommendations outlined in this article are as follows: the width of D is approximately dozens of times (such as 30 times) the width of the main lobe, while N's width is typically slightly wider than the target's width. For instance, if the detection targets are pipes or voids beneath a road, N is typically recommended to be less than 1 m. Certainly, these guidelines should be tailored to suit the real conditions.

The flow is illustrated as shown in Fig. 5, starting with the raw GPR data. In addition to conventional clutter removal techniques, the preprocessing phase is primarily dedicated to detecting of hyperbolas and layer interfaces. This phase involves advanced algorithms and methodologies tailored specifically for detecting these key geological structures, ensuring accurate identification and characterization. Considerable research effort has been directed toward the detection methods. The primary focus of this article is not on the discussion of the detection algorithm; rather, it elucidates its significance as an essential component of the preprocessing process. The estimation stage commences with the first layer, followed by the extraction of hyperbolas for testing. The BP algorithm, employing the proposed ray-based refraction method, is applied to the local region. This process involves iteratively testing a predefined set of permittivities as input parameters. The estimated permittivity depends on the focus metrics of these imaging results. This article uses image entropy as the focusing metric. According to the permittivity of the current layer and the previously detected layer range, the thickness also can be estimated naturally. The estimated parameter information is supplemented as the prior knowledge of the next layer. Once all layers have been traversed, the BP algorithm can be utilized to reconstruct the entire scene.

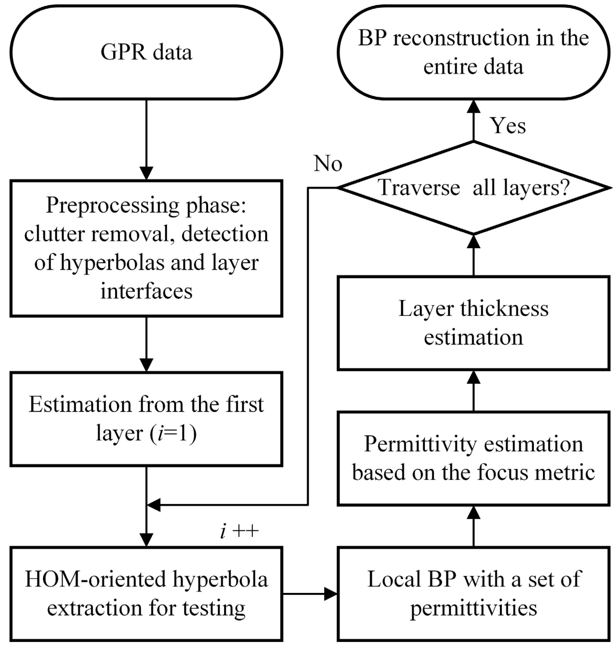

Fig. 5. Flow of the proposed HOM-oriented local BP estimation method. The iterative BP imaging process for permittivity estimation is performed only within the extracted local region.

III. FWM AND INVERSION

A. Forward Modeling

We utilized the FWM developed by Lambot et al. [25] and Lambot and André [38], which is applicable not only to planar layered media but also to other configurations. The backscattered field over the antenna aperture is assumed to be homogeneous, which applies in far-field conditions. Consequently, an equivalent single electric dipole approximation is used to describe the antenna's radiation properties. By leveraging the linearity of Maxwell's equations, the wave propagation between the point source or field point and the radar transmission line reference plane is characterized using complex, frequency-dependent global reflection, and transmission coefficients, as shown

$$\begin{bmatrix} -1 & A_2 & 0 & 0 & \dots & 0 & 0 & 0 \\ B_3 & -1 & A_3 & 0 & \dots & 0 & 0 & 0 \\ 0 & B_4 & -1 & A_4 & \dots & 0 & 0 & 0 \\ \vdots & \vdots & \vdots & \vdots & \ddots & \vdots & \vdots & \vdots \\ 0 & 0 & 0 & 0 & \dots & B_{n-1} & -1 & A_{n-1} \\ 0 & 0 & 0 & 0 & \dots & 0 & B_n & -1 \end{bmatrix} \begin{bmatrix} x_1 \\ x_2 \\ x_3 \\ \vdots \\ x_{n-2} \\ x_{n-1} \end{bmatrix} = \begin{bmatrix} -B_2 x_0 \\ 0 \\ 0 \\ \vdots \\ 0 \\ -A_n x_n \end{bmatrix} \tag{14}$$

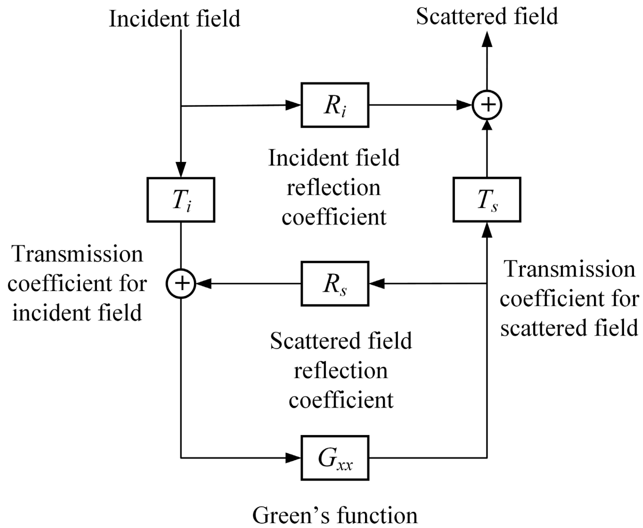

Fig. 6. Linear block diagram representing the far-field antenna model with global reflection and transmission coefficients that describe wave propagation between the radar reference plane and the source or field point [25].

in Fig. 6. These coefficients are crucial for determining the internal transmissions and reflections within the antenna and transmission line, thus influencing the antenna–medium interactions. Given a one-port vector network analyzer (VNA) as the radar system, the radar equation in the frequency domain is described as follows:

$$S_{11}(\omega) = R_i(\omega) + \frac{T(\omega)G_{xx}(\omega)}{1 - G_{xx}(\omega)R_s(\omega)} \tag{18}$$

where $S_{11}(\omega)$ is the measured radar signal by the VNA, $R_i(\omega)$ is the global reflection coefficient of the antenna for fields incident from the radar reference plane, $R_s(\omega)$ is the global reflection coefficient for fields incident from the antenna phase center, and $T(\omega) = T_i(\omega)T_r(\omega)$ is the antenna's global transmission coefficient. $G_{xx}(\omega)$ represents Green's function as the exact solution of the 3-D Maxwell's equations for wave propagation in multilayered media, and ω is the angular frequency. Notably, in free-space conditions, $G_{xx}(\omega) = 0$, thus, $S_{11}(\omega) = R_i(\omega)$, indicating that a free-space measurement directly provides $R_i(\omega)$.

Green's function can be directly calculated from the radar measurements using the radar-antenna characteristic functions

$$G_{xx}(\omega) = \frac{S_{11}(\omega) - R_i(\omega)}{T(\omega) + S_{11}(\omega)R_s(\omega) - R_i(\omega)R_s(\omega)}. \tag{19}$$

This equation yields a normalized quantity, the Green function, that is independent of the radar system. It mitigates undesired effects, such as antenna internal and antenna–medium multiple reflections. Therefore, the essence of removing the antenna effects is to solve for G_{xx} from (19). In the experiment, the reflection and transmission coefficients are constructed through multiple measurements on a perfect conductor to solve for G_{xx}. The process was introduced in [25] and was addressed in [24], for both far-field and near-field conditions.

B. Inverse Problem Formulation

Inversion can be performed in the frequency or time domain. The benefit of the time domain is that inversion can be focused on a time window, ignoring later reflectors, and making the inverse problem simpler. For instance, inversion focused on the surface reflection only would lead to only two unknowns, namely, antenna height and medium permittivity [32]. The frequency domain Green's function data are transformed into the time domain using the inverse Fourier transform

$$g_{xx}(t) = \mathcal{F}^{-1}\{G_{xx}(\omega)\} = \frac{1}{2\pi}\int_{-\infty}^{\infty} G_{xx}(\omega)e^{j\omega t}d\omega. \tag{20}$$

A maximal time $t_{\max}$ is set to isolate the surface reflection. The objective function is

$$\phi(\mathbf{b}) = \left(\mathbf{g}^*_{\mathbf{xx}} - \mathbf{g}_{\mathbf{xx}}\right)^T \mathbf{C}^{-1}\left(\mathbf{g}^*_{\mathbf{xx}} - \mathbf{g}_{\mathbf{xx}}\right) \tag{21}$$

where

$$\mathbf{g}^*_{\mathbf{xx}} = g^{\uparrow *}_{xx}(t)\big|_0^{t_{\max}} \quad \text{and} \quad \mathbf{g}_{\mathbf{xx}} = g_{xx}(t, \mathbf{b})\big|_0^{t_{\max}} \tag{22}$$

are the vectors containing, respectively, the observed and simulated time-domain windowed Green functions.

The objective function depends on the parameter vector $\mathbf{b} = [h, \varepsilon_r]$, where h is the antenna height above the ground and ε_r is the soil dielectric permittivity. We assume that soil's magnetic permeability is equal to free space permeability and negligible electrical conductivity effect on the surface reflection, which is a correct assumption for frequencies above 100 MHz [32], [39].

The objective function (21) indirectly relates the response function of the multilayered medium to its constitutive parameters. However, similar to most electromagnetic inverse problems, this function is usually highly nonlinear and exhibits oscillatory behavior with numerous local minima. In this article, for layers containing targets, we propose using the BP algorithm to provide a good initial model for FWI with the NMS algorithm [30], a classical local optimization algorithm, thereby enhancing the robustness while improving the computational efficiency of the local optimization algorithm. When encountering target-free layers, we use the global optimization by MCS [40] sequentially combined with the classical NMS to minimize (21).

IV. Synergistic Reconstruction Approach of BP and FWI in Unknown Multilayered Environments

In this section, we present a synergistic approach of BP and FWI, aiming at enhancing subsurface reconstruction accuracy in unknown multilayered environments. The processing pipeline is shown in Fig. 7. As an initial step in data processing, FWM is used to remove the antenna effects, followed by noise removal to enhance signal clarity. Subsequently, an essential procedure involves the detection of hyperbolas and layer interfaces within the radar image. Precise interface positioning is not required, as detailed calculations are handled in the FWI stage. Interface detection involves rough area division, achieved through manual judgment or the Hilbert transform. In this case, averaging B-scan data to obtain an A-scan helps detect the layer interface by accumulating data, making it more identifiable in sparse environments.

Considering the prevalent utilization of air–ground coupling antennas in practical detection, as used in this article, it is established that the relative permittivity of the first layer is 1. Furthermore, the determination of the first layer's thickness is roughly achievable through the analysis of the ground-reflected wave. Consequently, detection procedures commence from the second layer. In infrastructure environments characterized by the frequent deep burial of targets, it is crucial to recognize the lack of assurance regarding target presence across all layers. Consequently, it becomes imperative to guide the subsequent processes based on the presence or absence of a hyperbola within each layer. If hyperbolas are identified within the current layer, the proposed HOM-oriented local BP algorithm is employed to generate a preliminary estimation and establish an initial parameter model for the accurate FWI with NMS. Then, the mean values of the FWI results serve as the prior parameters for the BP algorithm in the next layer. Notably, while the BP algorithm provides estimations of permittivity and layer thicknesses for each layer, FWI outputs the permittivity of the nth layer and the thickness of the $(n-1)$th layer. If no hyperbola is detected in the current layer, traditional FWI with MCS and NMS is used for parameter estimation. Upon traversing all layers, the BP algorithm reconstructs each layer, augmenting its results with the layer interface information obtained from FWI to enhance the resolution of details.

In this article, we deal only with far-field conditions for the sake of simplicity. However, in many GPR applications, on-ground GPR is necessary to achieve sufficient penetration depth and resolution. The proposed method can also be applied in near-field conditions, but the near-field full-wave radar equation remains relatively complex to apply in practice [41]. Since the BP algorithm is based on the ray principle, it is applicable to both near-field and far-field scenarios, with the algorithmic process remaining consistent across these contexts. As a result, the proposed method is expected to be well-suited for engineering detection in both environments.

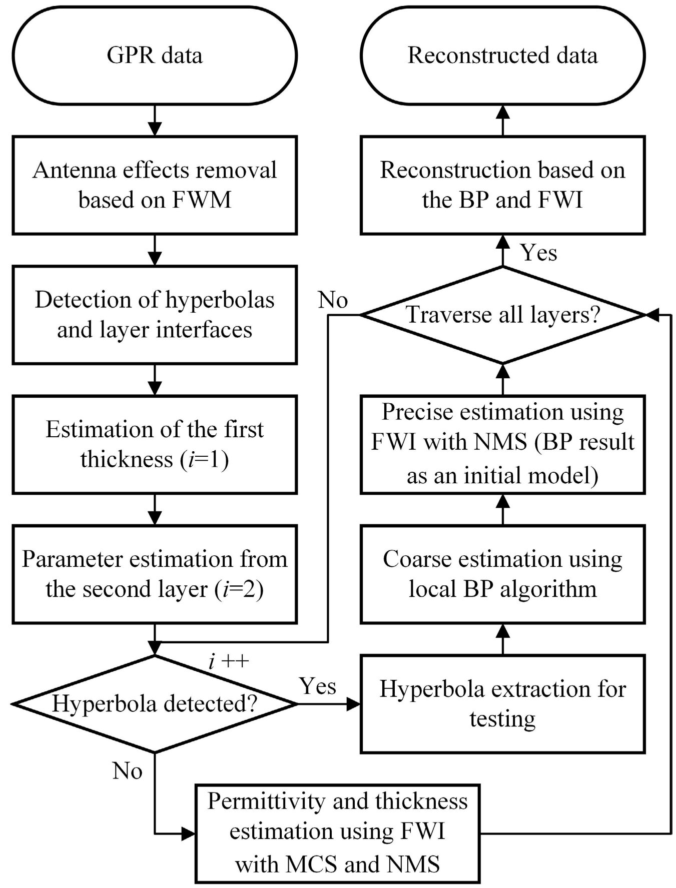

Fig. 7. Synergistic reconstruction approach combining BP and FWI in unknown multilayered environments. First, apply FWM to remove the antenna effects and detect hyperbolas and layer interfaces. Then, estimate parameters layer-by-layer: if a hyperbola is detected, apply the BP algorithm for initial estimation, followed by FWI with NMS for precision. If not, proceed directly with FWI using MCS and NMS for estimation. Finally, reconstruct the scene.

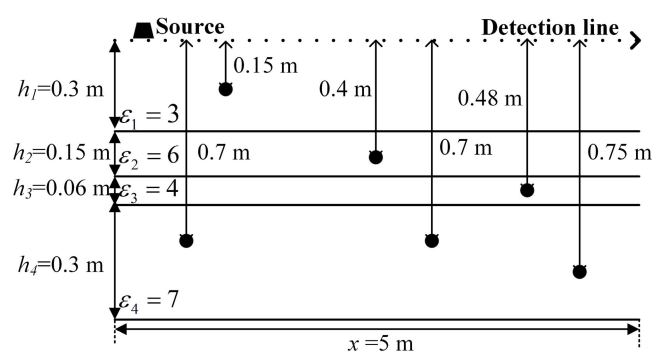

Fig. 8. Four-layer model. The dipole point source is moved along the detection line with a step size of 0.01 m. The necessary parameters required by the BP algorithm, such as layer thickness and relative permittivity, are indicated in the corresponding layer. At least one point target is placed in each layer, and its corresponding depth is provided.

V. Simulation Results and Analysis

A. Simulated Data

In the simulation experiment, a four-layer model was simulated, as illustrated in Fig. 8. A dipole point source with a center frequency of 1.5 GHz is positioned near the ground surface, with measurements taken at 5 m, using a sampling interval of 0.01 m and a time window of 15 ns. The unit grid size in gprMax is 0.005 m in all three dimensions. The thicknesses of the four layers are 0.3, 0.15, 0.06, and 0.3 m, respectively, with relative permittivities of 3, 6, 4, and 7. Each of the first three layers contains one target, while the last layer contains three targets. The depths of these targets are annotated in the model, and their relative permittivities are randomly distributed between 1 and 7. All targets are point targets with a diameter of 0.01 m.

Fig. 9 presents the preprocessed echoes from the simulation data. In Fig. 9(a), the averaged A-scan echo is shown. Because the time delays and intensities of the interface echoes are identical across each A-scan, these interfaces are clearly captured. The specific positions of the interfaces were detected using the Hilbert transform [42], [43]. Fig. 9(b) illustrates the hyperbolic responses of the point targets after the removal of horizontal clutter, with the positions of the hyperbolic vertices detected using Mertens's automatic detection algorithm [44]. It can be observed that to highlight the targets, horizontal responses are removed during preprocessing, which makes it difficult to provide detailed information about the interfaces. For clarity, we combined the averaged A-scan and the

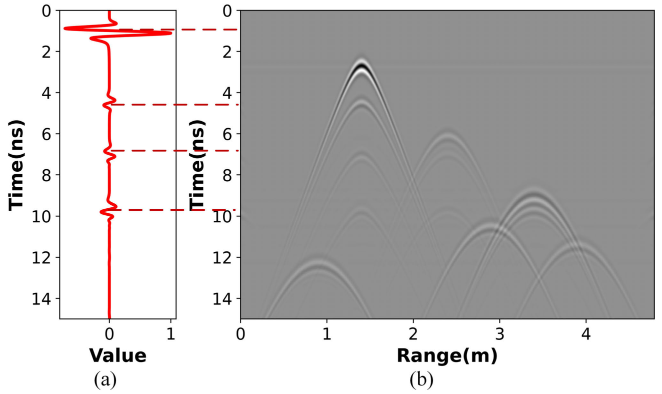

Fig. 9. Preprocessed and HOM window-based hyperbola extraction results. (a) Averaged A-scan and (b) target data and extraction results.

preprocessed B-scan and annotated the exact positions of the interfaces within the B-scan.

In Fig. 9(b), the red box highlights the object extracted for estimation by the HOM window. The HOM window has a horizontal width of 0.6 m and a vertical length of 3.53 ns. Among the three targets in the fourth layer, the HOM window selects the left hyperbola. A visual comparison reveals that, unlike the other two hyperbolas which are affected by the trailing edges of the upper hyperbola, the extracted hyperbola has a cleaner background. This is also reflected in the HOM values of the three targets: 7.50, 6.77, and 6.81.

Fig. 10 provides a detailed illustration of the estimation process of the four-layer model. The local imaging range of each layer corresponds to the width of the extracted hyperbolic HOM window and the length of the layer. The iterative process initializes the relative permittivity from 1 to 15 for a total of 20 iterations. Fig. 10(a)–(d) represent the four layers of the medium, while (i)–(iii) depict the imaging results of the relative permittivity at the beginning, estimated value, and end of the estimation process, respectively. The iterative process follows a pattern of hyperbolas bending upward, focusing, and then bending downward, regardless of the layer. The estimated relative permittivities of the four layers are 3.25, 6.05, 4.33, and 6.05, with absolute errors of 0.25, 0.05, 0.33, and 0.95, and the relative errors of 8.33%, 0.83%, 8.25%, and 13.57%, respectively. The thicknesses of the first three layers are 0.30, 0.15, and 0.06 m, without error. The overall runtime is 1228.24 s. The experimental setup utilized a computer with the following specifications: AMD Ryzen 5 3550H with Radeon Vega Mobile Gfx clocked at 2.10 GHz, equipped with 16.0 GB of RAM. Fig. 11 reconstructs the entire four-layer environment based on the estimation results, with each hyperbola achieving excellent focus in the image.

To further analyze the proposed ray-based refraction method in multilayered media, we established a two-layer model based on common structural parameters of roads and the characteristics of GPR detection [45], [46]. We then analyzed the average error during the estimation of refraction points, as shown in Tables I and II. In the two-layer model set-up, the thicknesses of the first layer (h_1) and the second layer (h_2) ranged from 5 to 50 cm, while the detection distance of the antenna varied from 0 to 50 cm. Table I illustrates the

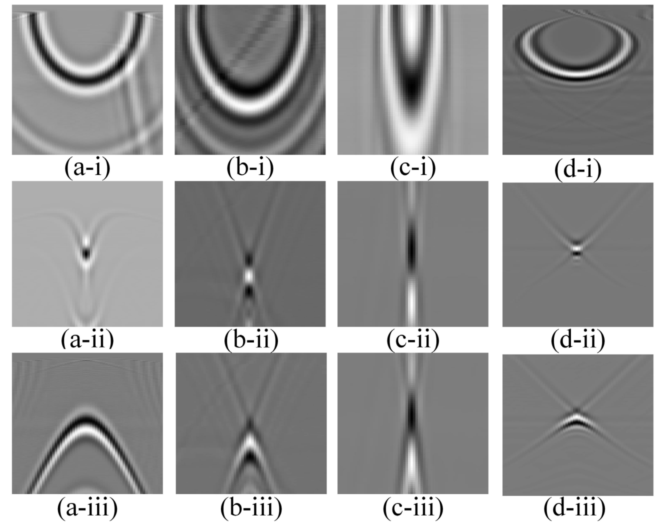

Fig. 10. Local BP estimation results. (a)–(d) Four layers, while (i)–(iii) depict the imaging results of the relative permittivity at 1, the estimated value, and 15, respectively.

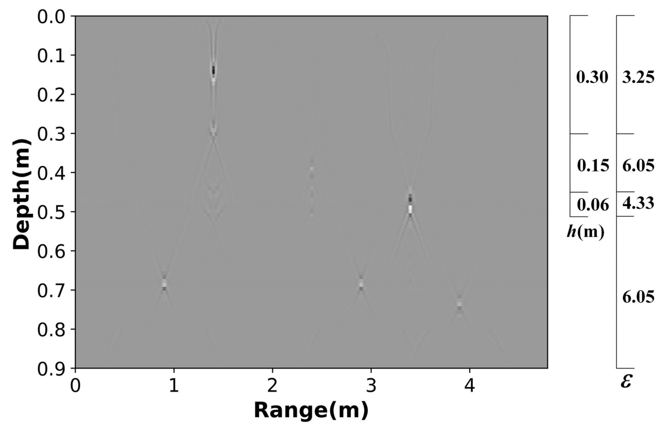

Fig. 11. Reconstruction of the simulated environment. All the hyperbolas are focused well, accurately indicating the location of each target.

average error of the proposed algorithm when the permittivity decreases ($0 < \widetilde{\varepsilon} < 1$). Table II illustrates the average error of the proposed algorithm when the permittivity increases ($1 < \widetilde{\varepsilon} < 15$).

The two tables illustrate the calculation errors of refractive points under varying thickness combinations of h_1 and h_2 of the medium. In the case of $0 < \widetilde{\varepsilon} < 1$, the average error fluctuates across different combinations of h_1 and h_2. For instance, when both h_1 and h_2 are 5 cm, the error is 3.46 cm, whereas for h_1 and h_2 both set to 5 cm, the error reduces to 0.08 cm. Overall, an increase in h_1 and h_2 leads to a gradual decrease in error, indicating a positive influence of thickness on the accuracy of refractive point calculations. When $1 < \widetilde{\varepsilon} < 15$, a similar trend is observed with a decreasing average error as h_1 and h_2 increase. However, the error values here are generally smaller compared with Table I, suggesting a relatively higher precision of the model across different thickness combinations. For instance, when both h_1 and h_2 are 5 cm, the error is 3.10 cm, slightly lower than the corresponding value in Table I.

TABLE I

AVERAGE ERROR (CM) AT $0 < \widetilde{\varepsilon} < 1$. THE TOTAL AVERAGE ERROR IS 1.03 CM. THE MINIMUM ERROR OCCURS AT $h_1 = 5$ CM AND $h_2 = 50$ CM, WHILE THE MAXIMUM ERROR OCCURS AT $h_1 = 50$ CM AND $h_2 = 5$ CM

h1 \ h2	5	10	15	20	25	30	35	40	45	50	avg.
5	3.46	1.68	0.94	0.58	0.38	0.26	0.19	0.14	0.11	0.08	0.78
10	3.01	1.64	0.99	0.63	0.42	0.29	0.21	0.16	0.12	0.09	0.76
15	2.21	1.30	0.82	0.55	0.38	0.27	0.20	0.16	0.13	0.10	0.61
20	1.70	1.05	0.70	0.50	0.37	0.29	0.23	0.19	0.16	0.15	0.54
25	1.60	1.04	0.75	0.58	0.47	0.40	0.35	0.31	0.28	0.26	0.60
30	1.84	1.31	1.02	0.84	0.72	0.62	0.55	0.49	0.44	0.40	0.82
35	2.28	1.74	1.41	1.18	1.01	0.88	0.77	0.68	0.60	0.55	1.11
40	2.81	2.21	1.81	1.52	1.30	1.12	0.99	0.87	0.78	0.70	1.41
45	3.31	2.64	2.18	1.83	1.58	1.37	1.20	1.06	0.94	0.85	1.70
50	3.75	3.02	2.51	2.12	1.83	1.59	1.40	1.24	1.11	1.00	1.96
avg.	2.60	1.76	1.31	1.03	0.85	0.71	0.61	0.53	0.47	0.42	1.03

TABLE II

AVERAGE ERROR (CM) AT $1 < \widetilde{\varepsilon} < 15$. THE TOTAL AVERAGE ERROR IS 1.38 CM. THE MINIMUM ERROR OCCURS AT $h_1 = 50$ CM AND $h_2 = 5$ CM, WHILE THE MAXIMUM ERROR OCCURS AT $h_1 = 5$ CM AND $h_2 = 50$ CM

h1 \ h2	5	10	15	20	25	30	35	40	45	50	avg.
5	3.10	3.11	2.68	2.32	2.19	2.34	2.78	3.48	4.36	5.21	3.16
10	1.61	1.79	1.62	1.47	1.48	1.72	2.21	2.91	3.65	4.34	2.28
15	0.95	1.11	1.04	0.99	1.07	1.36	1.86	2.48	3.09	3.67	1.76
20	0.61	0.72	0.70	0.70	0.83	1.13	1.62	2.14	2.66	3.15	1.43
25	0.41	0.49	0.49	0.52	0.67	0.98	1.42	1.86	2.30	2.73	1.19
30	0.28	0.35	0.36	0.41	0.57	0.87	1.25	1.63	2.01	2.39	1.01
35	0.21	0.25	0.27	0.33	0.49	0.78	1.11	1.44	1.78	2.10	0.88
40	0.15	0.19	0.21	0.28	0.44	0.70	0.99	1.28	1.57	1.87	0.77
45	0.12	0.14	0.16	0.24	0.41	0.64	0.88	1.14	1.41	1.67	0.68
50	0.09	0.11	0.13	0.21	0.37	0.58	0.80	1.03	1.26	1.50	0.61
avg.	0.75	0.83	0.77	0.75	0.85	1.11	1.49	1.94	2.41	2.86	1.38

However, when the thickness of the first layer h_1 is 5 cm, the average error in refraction point calculation can reach 3.16 cm, and the maximum error can reach 5.21 cm at $h_2 = 50$ cm. This indicates that when thin layers are present in the environment, errors in refraction point calculation will severely affect the parameter estimation of deeper layers and subsequent scene reconstruction. Combining the estimation process shown in Fig. 10(c-i)–10(c-iii), we can observe that in thin layer environments, due to the variation of parameters during the estimation process, hyperbolas may appear to move up or down, resulting in incomplete imaging within the window. Therefore, we should try to avoid using the BP algorithm for estimation in thin layers. In addition, in actual road conditions, thin layers typically occur near the surface, with earlier echo delays [47]. Therefore, in this case, it is recommended to use FWI for parameter estimation. To avoid failure of imaging in the underlying layers, an effective approach is to combine them with other layers and consider the permittivity as the average permittivity, serving as prior knowledge for imaging the lower layers. Specific procedures are detailed in the field measurement section.

VI. SANDBOX LABORATORY EXPERIMENT

A. GPR System and Sandbox Configuration

The sandbox laboratory experiment was conducted at the Georadar Research Center of the Université catholique de Louvain (http://sites.uclouvain.be/gprlouvain) to evaluate the proposed synergistic approach. This experiment was initially setup in the frame of the study of [24]. The GPR system consisted of a stepped-frequency continuous-wave (SFCW) radar system set up with a VNA from Rohde & Schwarz, headquartered in Munich, Germany. The antenna was a single transmitting and receiving, a linearly polarized, double-ridged broadband horn antenna (BBHA 9120 A) sourced from Schwarzbeck Mess-Elektronik, Schönau, Germany. The antenna possessed dimensions of 195 mm in height and an aperture measuring 142 × 245 mm. Operating within a nominal frequency range of 0.8–5.0 GHz, the antenna boasted isotropic gain capabilities ranging from 6 to 18 dB. Its notable directivity, with a 45° 3 dB beamwidth in the E-plane and 30° in the H-plane at 1 GHz, conferred immunity to external interferences or reflections. Connection to the VNA's reflection port was established via a high-quality n-type 50-Ω coaxial cable, with calibration performed at the interface between the antenna feed point and the cable utilizing an open-short-match calibration kit. Frequency-dependent complex ratios $[S11(\omega)]$ between incident and backscattered waves at the radar reference plane were measured across 1601 frequencies spanning 800–4000 MHz, with a frequency increment of 2 MHz.

Radar measurements were conducted within a 3 × 3 m sand box, as shown in Fig. 12. Tran et al. [48] demonstrated that the far-field assumption is valid when the antenna height is at least 1.2 times its aperture size. Accordingly, the antenna aperture was positioned approximately 0.3 m above the sand surface to ensure far-field conditions were met. A copper sheet, emulating a perfect electrical conductor (PEC), was embedded at the base of the 0.86-m-thick sand layer to maintain controlled boundary conditions. The targets of interest comprised three PVC pipes, each measuring 1.20 m in length, 50 mm in diameter, and with a thickness of 1.8 mm, buried at depths of 0.07, 0.29, and 0.51 m, respectively. These pipes were aligned in parallel orientation, with horizontal distances from the B-scan starting point equating to approximately 0.47, 1.17, and 1.97 m, respectively. Each pipe contained air as its fill material. The radar system was affixed to an XYZ automated positioning table to facilitate systematic data acquisition along a 2.40-m profile, with positional increments of 1 cm. Notably, the radar profile was transverse to the orientation of the pipes. The calibrated phase center of the antenna is located at 0.0714 m from the bottom of the antenna. Hence, the thickness of the first layer is actually 0.3714 m.

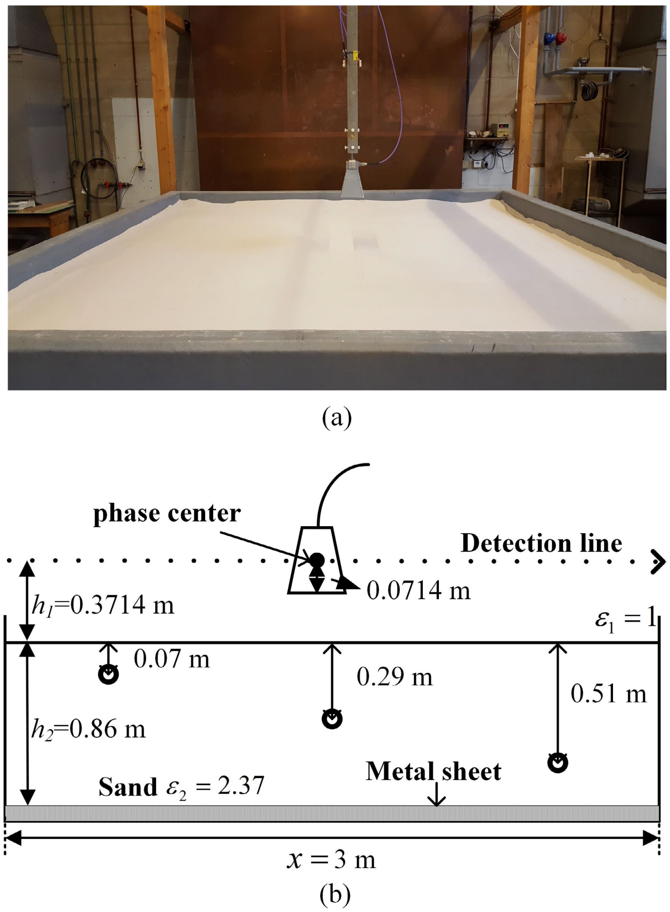

Fig. 12. Sandbox laboratory experiment. (a) Sandbox and the antenna and (b) configuration details. The 3 × 3 m copper sheet visible in the background served as a PEC for calibrating the antenna, namely, for determining its characteristic functions following the full-wave radar equation.

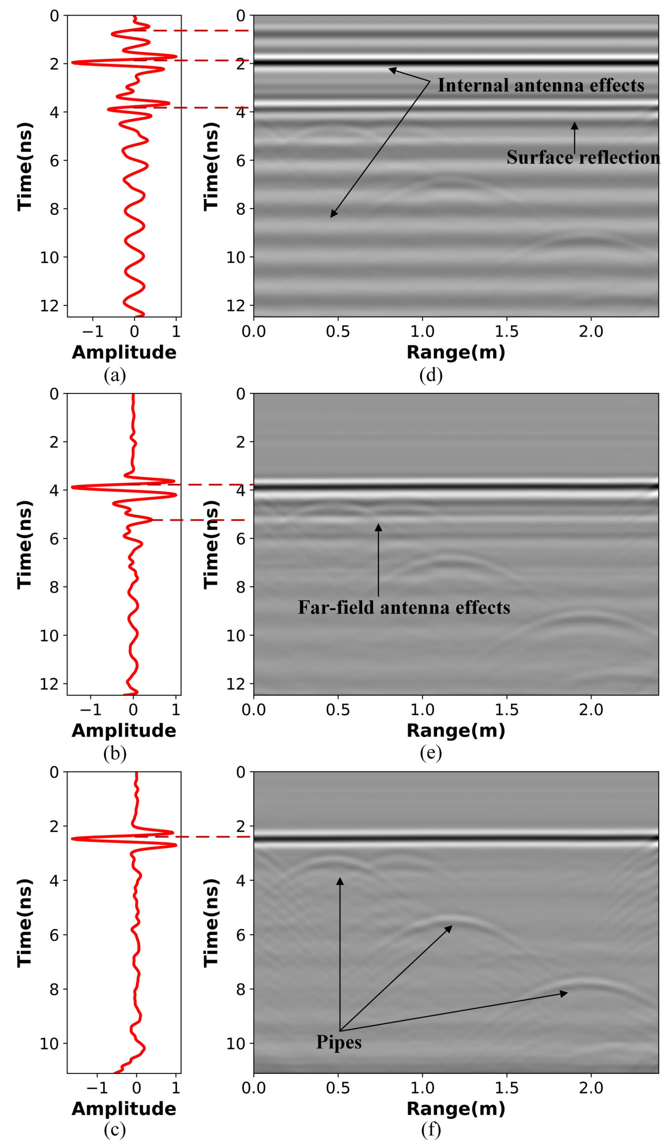

Fig. 13. Comparison of data before and after antenna effect removal. (d)–(f) Original data, the results after removing the internal antenna effect, and the results after removing the far-field antenna effect, respectively. (a)–(c) Corresponding first A-scan data for each case.

B. Experimental Results and Analysis

In the sandbox experiment, we applied a time window to focus on the layers above the metal sheet, which produced a strong reflection at a greater depth. This allowed us to concentrate on the antenna effects and parameter inversion in the relevant layers. Fig. 13 visually shows the comparison of the data before and after eliminating the multiple echoes from the antenna. Fig. 13(d) shows the raw echo data collected directly, where it is difficult to identify the target echoes due to strong horizontal clutter, which is from the internal antenna effects. These echoes have very high intensity due to internal reflections within the antenna, completely overwhelming the real scene. After removing the free-space response of the antenna R_i, Fig. 13(e) shows that most of the repetitive horizontal clutter has been eliminated, with the strongest echo now corresponding to the reflection from the surface of the sand. However, in the later time delay, multiple reflections can still be observed, particularly a distinct reflection at 5 ns caused by multiple reflection within the antenna from the backscattered medium echo. If not removed, this reflection, and some others later, could easily be misinterpreted as indicating a layered environment within the sandbox, thereby misleading subsequent processing tasks. Fig. 13(f) shows the results after completely removing both types of clutter and correcting the zero time using the far-field radar (19). The three pipe targets are clearly visible, with a faint reflection next to the uppermost pipeline, likely caused by impurities within the sand. Fig. 13(a)–(c) shows the averaged A-scan echoes corresponding to the B-scan data. The impact of the aforementioned multiple reflections and the detected interface positions can be seen more clearly in these figures.

Fig. 14 presents the results based on the proposed HOM-oriented local BP estimation method. The hyperbolas extracted for estimation, marked within the red box, are based on the HOM window. The calculated results for the four hyperbolas within the HOM window are 6.24, 3.08, 8.64, and 8.52, respectively. The relative permittivity to be tested was set from 1 to 15, with a total of 20 iterations. Fig. 14(b)–(d) illustrates the variation of the permittivity from low to high throughout the iterations. Fig. 14(c) displays the result with the optimal focusing index, where the estimated relative

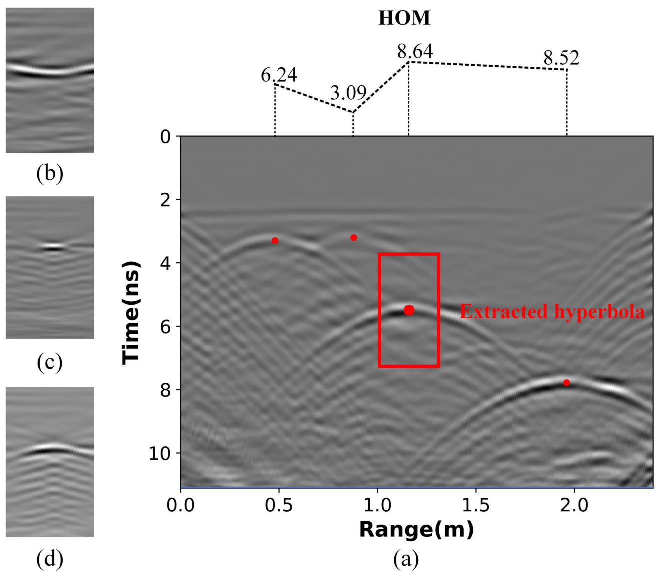

Fig. 14. Results of hyperbola extraction based on (a) HOM-window and (b)–(d) local BP estimation results for the laboratory experiment.

permittivity is 2.53, which is in agreement with the expected value for a dry loose sand. The relative error is 6.75%, and the absolute error is 0.16. The thickness of the first layer is 0.357 m. The running time is 75.43 s.

Based on the proposed synergistic GPR approach of BP and FWI, we input the local BP estimation results, thickness of 0.357 m, and relative permittivity of 2.53, into the FWI with NMS. The inversion results are shown in Fig. 15. Fig. 15(b)–(d), respectively, describes the thickness variation from the antenna to the sand surface, the detected relative permittivity of the sand, and the fitting results of the first A-scan data. The average thickness is 0.366 m, and the average relative permittivity is 2.50. The relative error of FWI with NMS is 5.49%, which is an improvement of 1.26% compared with the BP estimation results. The running time for the FWI with NMS is 3633.80 s. Including the BP estimation time, the total runtime is 3709.23 s. In contrast, the FWI with MCS and NMS results in a running time of 37829.77 s, which is ten times the running time of the combination of BP and FWI. This demonstrates the superior efficiency and effectiveness of the proposed method.

By integrating the BP and FWI estimation results, the final reconstruction of the scene is obtained, as shown in Fig. 15(a). It is evident that both the point targets and the interface information can be clearly depicted. FWI revealed detailed variations in the sand surface thickness, ranging from thick to thin. A subtle increase is observed in the interface height from left to right, which is challenging for the BP algorithm to reconstruct. However, BP compensates by providing crucial target information.

Fig. 15(e)–(l) illustrates the impact on parameter estimation and reconstruction using BP and FWI without removing the antenna effects. If parameter estimation is performed directly on the raw data, we can at least identify four layers of media, as shown in Fig. 13(a) and (d). Since there are no targets in the first three layers, the FWI with MCS and NMS is used, and the estimation results for each layer are shown in Fig. 15(f)–(h). It can be observed that the thickness and relative permittivity variations are significant in each inversion layer, and the fitting results of the first A-scan data also indicate that correct parameters are difficult to invert in this scenario. The average relative permittivities of the last three layers are 0.99 (which is nonphysical), 1.04, and 1.20, respectively. The average thicknesses of the first three layers are 0.46, 1.42, and 0.32 m, respectively. Fig. 15(e) demonstrates that inputting these results into the BP algorithm fails to accomplish the reconstruction task.

For the data shown in Fig. 13(e), three layers of media are clearly detected. Since there are point targets in both the second and third layers, the BP algorithm can be directly used for estimation and then utilize the FWI with NMS for further estimation, as shown in Fig. 15(i)–(l). The BP algorithm yields average relative permittivity estimates of 9.05 and 11.47 for the last two layers, with thicknesses of 0.57 and 0.12 m for the first two layers, respectively, which deviate significantly from the actual configuration. Obviously, in the subsequent FWI algorithm results, it can be observed that such initial models are even less likely to obtain parameters close to the real situation. The average relative permittivities are 1.05 and 1.00, and the average thickness values are 1.70 and 0.16 m. Clearly, such estimation results are far from the actual scene.

From the sandbox experiment, we have validated the effectiveness of the proposed GPR reconstruction algorithm combining BP and FWI. We particularly emphasized the analysis of the influence of antenna effects on the estimation and reconstruction process. Next, let us proceed to the real road experiment, where we will further discuss the effectiveness, limitations, and corresponding solutions of the proposed algorithm in practical applications.

VII. Belgian Road Research Centre (BRRC) Experiment

A. Test Site Description and Data Acquisition

Measurements were conducted within the facilities of the BRRC located in Wavre, Belgium [49]. The test site, depicted in Fig. 16, comprises four sections, each 1.7-m wide, distributed along an 11.5-m-long profile. Zones 1 and 2 represent the typical pavement structures found in Belgium, featuring asphalt layers overlying concrete and lean concrete, respectively. The remaining areas, a and c zones, serve as transitional zones necessary for constructing the aforementioned road structures and other facilities not mentioned. Various utilities, including dowels, temperature sensors, and 10-cm-long strain gauges, were intentionally buried in zones a and c. Zone 1 replicates a void beneath a concrete slab, whereas zone c simulates an artificial slope and an adhesion defect between two bituminous layers. Pavement layer thicknesses were monitored throughout the construction process using topographic measurements. The nominal thicknesses and the measured thicknesses are summarized in [49]. The combined thickness of the two asphalt layers in zones 1 and 2 is slightly less (5–6 mm) than the initially planned thickness (10 cm). Discrepancies between the expected and measured values may

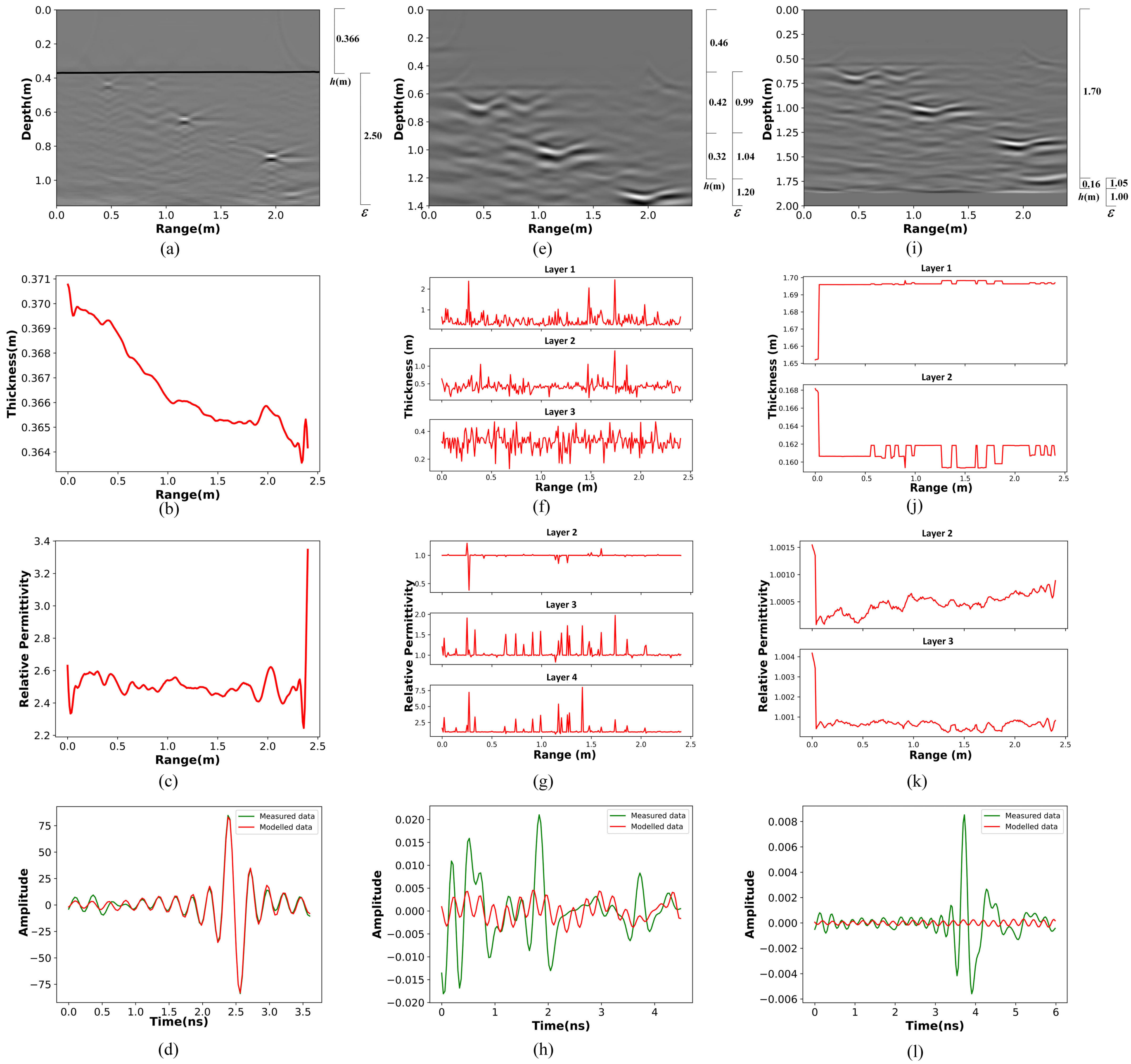

Fig. 15. Reconstruction of the proposed synergistic GPR approach (a)–(d) with and (e)–(l) without removing the antenna effects. (a), (e), and (i) are the reconstruction images. (b), (f), and (j) are the thickness results from FWI. (c), (g) and (k) present the permittivity results from FWI.

stem from construction inaccuracies. The dataset was acquired along this site using the same radar system as in the sandbox experiment. The antenna was mounted at the rear of a van at an approximate height of 0.47 m above the pavement surface. The calibrated phase center of the antenna is located at 0.0714 m from the bottom of the antenna. An odometer attached to the rear wheel of the vehicle precisely determined the traveled distance and triggered GPR measurements at defined intervals (sampling density of 100 scans/m).

B. Reconstruction and Analysis

As this article focuses on data reconstruction in a horizontal layered environment, the radar data captured includes complete datasets from zones 1, 2, and a, as well as zone c, which contains strain gauges. Fig. 17 displays prominent interface reflections and several artificially placed target echoes. Within the echoes, four layers of media can be clearly discerned: the air layer, two asphalt layers, and the concrete layer. Due to signal attenuation and medium effects, the aggregates at the bottom cannot be distinctly detected. Fig. 18(a) presents the target-dominated data after removing horizontal clutter, along with detected hyperbolas. No targets exist in the first two layers of media, while two hyperbolas are present on the reflective surface of the fourth layer. However, as described in the simulation data experiment, selecting such targets for inversion may not fully capture the imaging results of the interface. Moreover, the echoes from the first three layers have earlier time delays, thus requiring

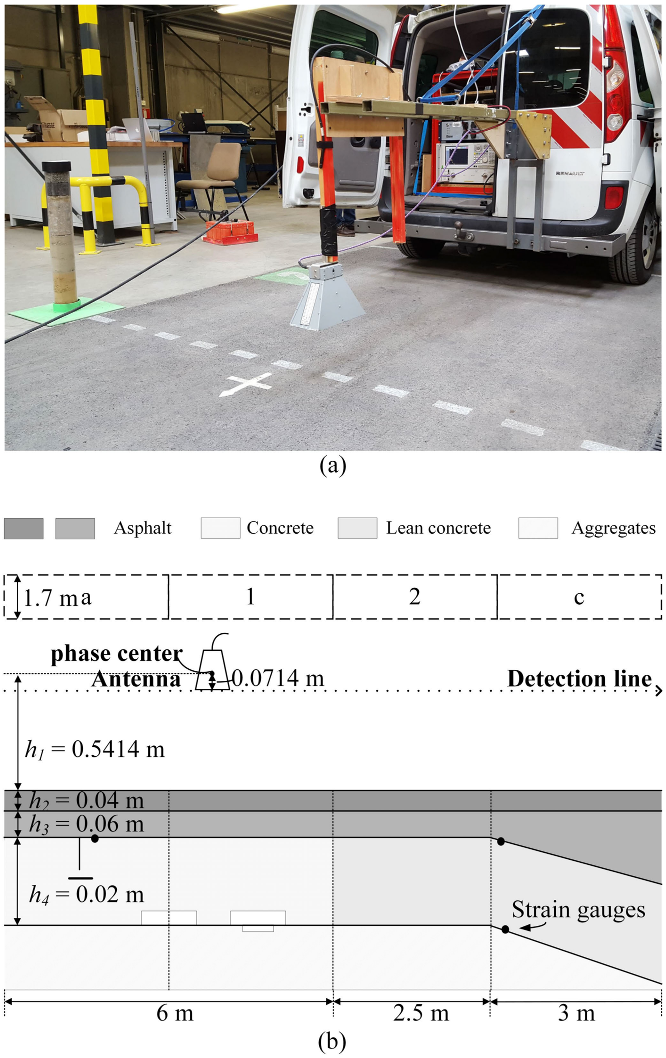

Fig. 16. Configuration of the BRRC test site (Wavre, Belgium) used in laboratory experiments. (a) Real test site and (b) design diagram of the scene.

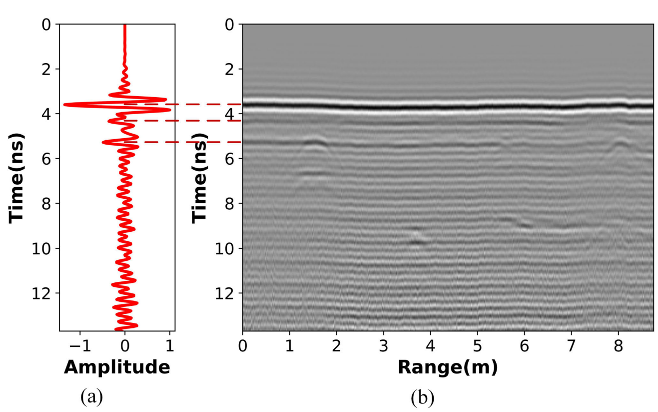

Fig. 17. B-scan data after removing the antenna effect using Green's function (b) and its average data (a). The internal effects of the antenna, as well as the interactions between the antenna and the medium, are removed, and the zero-time position is identified.

inversion using FWI with MCS and NMS. Therefore, in this dataset, our strategy involves employing FWI for the first three layers and a combination of BP and FWI for the fourth layer. Since the inversion of the first three layers of media is solely intended to provide prior knowledge for the BP algorithm, and BP only requires a single average value rather than the inversion result of each A-scan data, we invert the first A-scan data to obtain the relative permittivity of the first three layers: 1, 4.01, and 3.12, with layer thicknesses of 0.54, 0.05, and 0.05 m, respectively, which serve as the prior conditions for BP. It is worth noting that in this dataset, the thickness of the second and third layers is less than 0.1 m. According to the error analysis discussed earlier, it is highly likely that estimation failure may occur due to error propagation. Therefore, in practical operations, we consider the environment as a three-layer medium, where the original second and third layers are combined into one layer, resulting in a single layer with a thickness of 0.1 m and an average relative permittivity of 3.66.

After the local BP estimation, the relative permittivity of the last layer is determined to be 6.05. Subsequently, incorporating this value into the FWI with NMS, the inversion results are illustrated in Fig. 18(d)–(f). The average thicknesses of the first three layers are determined to be 0.55, 0.06, and 0.06 m, respectively. It is worth noting that the estimated thickness of 0.55 m includes the distance from the phase center to the bottom of the antenna, indicating that the actual height from the bottom of the antenna to the sand surface is 0.4786 m. The average relative permittivities of the last three layers are calculated to be 3.84, 4.19, and 4.7. The total running time is 25208.45 s. If we just apply the FWI with MCS and NMS to the four layers, the running time is 95048.90 s.

The scene reconstruction results are depicted in Fig. 18(c). Compared with Fig. 18(a), it is evident that all hyperbolas are well focused. In contrast to the reconstruction using BP alone as shown in Fig. 18(b), (c) incorporates layer interface information, resulting in a more refined reconstruction.

It is worth noting that the observed discrepancies for the deeper layers are to be attributed to: (1) the increased heterogeneity of the underlying materials, which introduces clutter and noise into the GPR echo data; 2) the ill-posed nature of the inverse problem when using a radar system with a single transmitter–receiver offset, making deeper layer reconstruction more challenging; and 3) the lower signal-to-noise ratio for reflections from deeper interfaces due to signal attenuation, which further reduces inversion accuracy.

When the scene is modeled as four layers, the BP algorithm result is shown in Fig. 19(a). While the imaging quality of the first three layers is satisfactory, some confusion arises in the fourth layer. In the final stage of this experiment, we used two simulation models to verify the feasibility of the issues encountered during the processing of the measured data and to evaluate the proposed solutions. Fig. 19(b) and (d) represent four-layer models based on experimental parameters, where the relative permittivities are consistent with the previously estimated values, but the layer thicknesses differ. Fig. 19(b) closely matches the actual layer depth, while the thickness of each layer in Fig. 19(d) is within a range that minimizes BP imaging errors. As shown in Fig. 19(c), the imaging results correspond with the measured data, suggesting that error propagation negatively impacts the imaging quality of the fourth layer. However, each layer of the target in

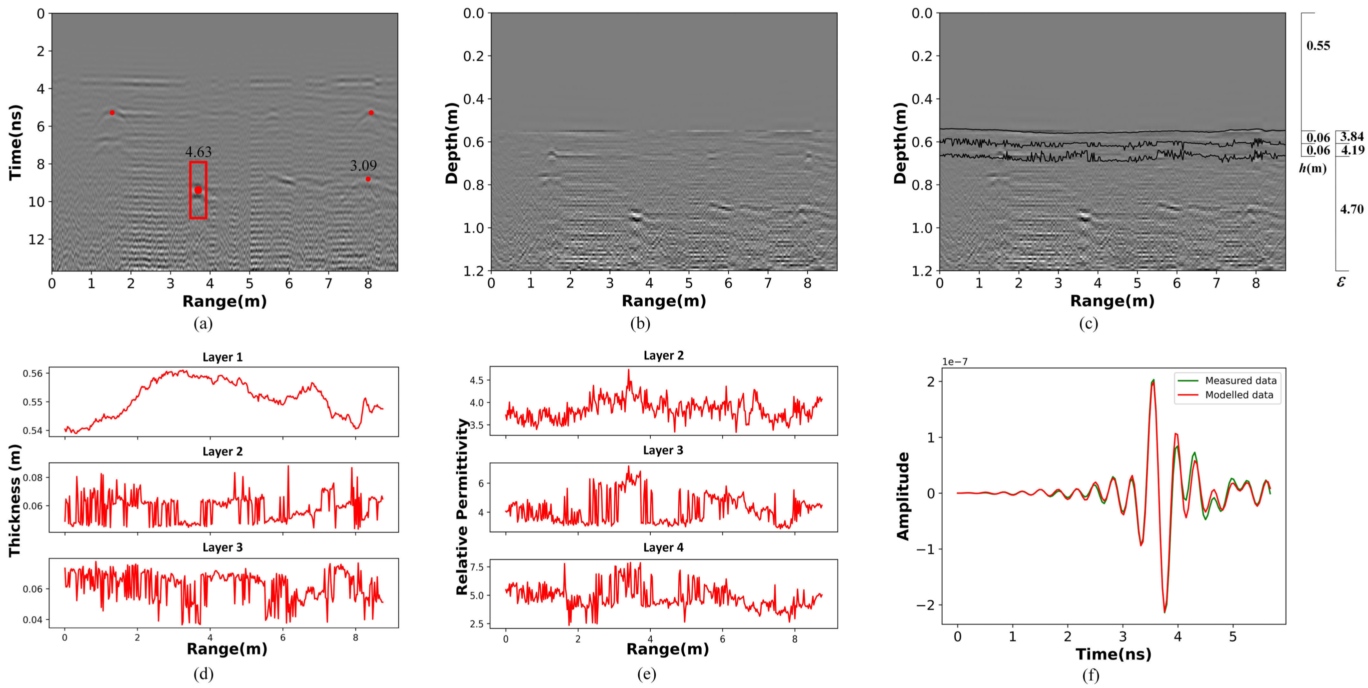

Fig. 18. Road data reconstruction results. (a) Preprocessed image with hyperbola extraction. (b) BP reconstruction results. (c) Final reconstruction integrated with FWI, highlighting the targets and layer interfaces. (d)–(f) Fitting results for thickness, relative permittivity, and first A-scan data obtained by FWI, respectively.

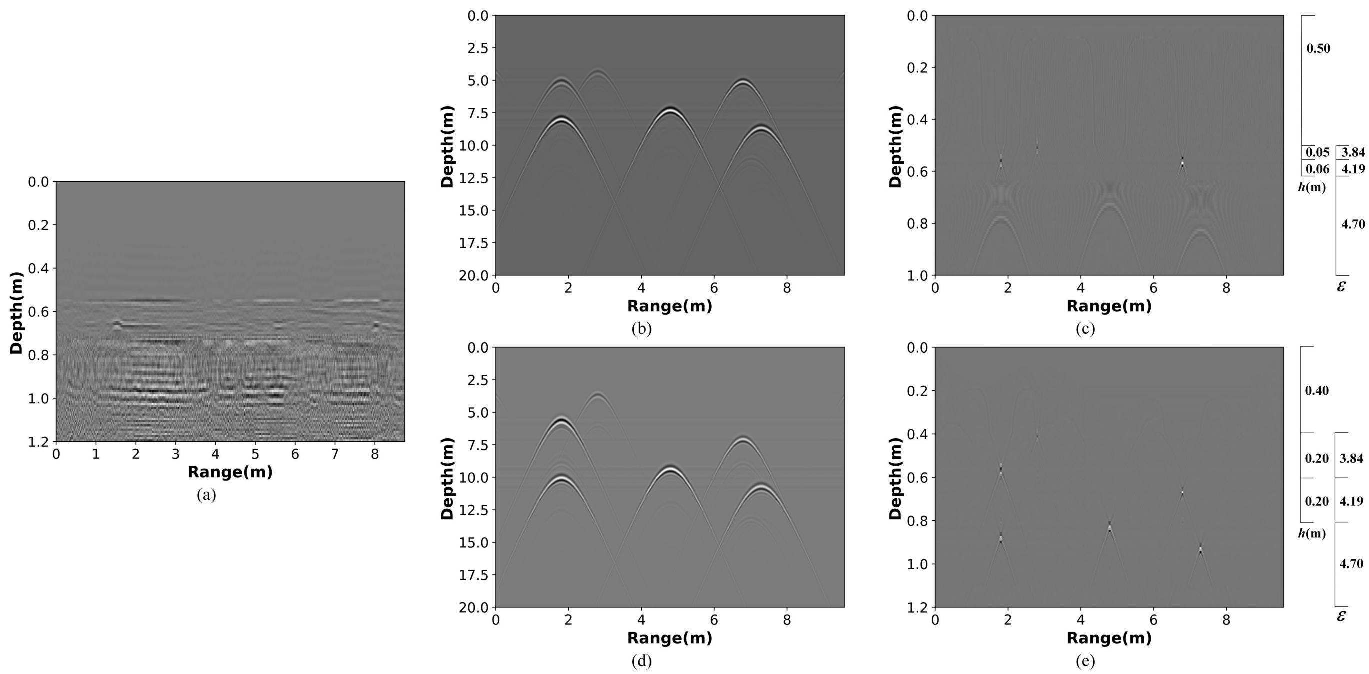

Fig. 19. Verification of the BP algorithm limitations. (a) Result of considering the BP model as a four-layer structure. (b) and (d) Show the preprocessed echoes of the model simulated based on the measured data. The relative permittivities match the measured data, with variations only in layer thickness. (b) Model closely aligned with the BP algorithm under restricted conditions and (d) depth comparisons within the reasonable range of BP accuracy. (c) and (e) Corresponding BP imaging results.

Fig. 19(d) is well-focused. This supplementary experiment further validates the effectiveness of the proposed method and strategy, enhancing the overall experimental findings.

VIII. Conclusion and Perspective

This article proposes a synergistic GPR approach combining the BP algorithm and FWI to reconstruct unknown layered environments such as roads. The proposed ray-based refraction method and HOM-oriented local BP enhance the computational efficiency of BP estimation and medium reconstruction by addressing the two critical processes in BP calculation: delay calculation and summation. Subsequently, the integration and interaction possibilities of the BP algorithm and FWI in parameter estimation and scene reconstruction are explored. The BP algorithm focuses on B-scan echoes, addressing spatial aspects by macroscopically estimating medium parameters through the focus variations of target hyperbolas with different parameters. It also provides a robust and efficient initial model for FWI, ensuring robustness and iterative efficiency in the minimization fitting process. FWI, based on A-scan data, focuses on the microscopic propagation of electromagnetic waves in each layer from the perspective of Green's function, to fit the parameters in the target-free layers, thus complementing the shortcomings of the BP algorithm relying on target hyperbolas and correcting its error propagation.

Three progressively sequential experiments were conducted: simulation validation, ideal sandbox experiments, and actual road detection. In the simulation experiments, the point source was substituted for antennas to verify the effectiveness of the BP algorithm in an ideal layered environment. The accuracy of the proposed algorithm in road detection scenarios was also summarized and discussed. The average errors of the proposed algorithm under experimental conditions were measured at 1.03 and 1.38 cm, respectively.

The sandbox experiments primarily investigated the influence of antenna multipath reflections on multilayered media reconstruction. Three sets of data were compared: raw echoes, echoes with free-space antenna response removed, and echoes with complete antenna effects removal using the full-wave radar equation. When all the reflections were effectively eliminated, the absolute error of the BP algorithm in terms of permittivity was 0.16, and after FWI correction, the absolute error was reduced to 0.13. However, using inadequately processed GPR data directly induced serious errors in layer calculation due to the influence of reflection clutter, ultimately leading to significant discrepancies between estimated results and actual conditions, rendering the reconstruction ineffective.

Finally, the real data from the BRRC was utilized to validate and discuss the practical engineering applications of the proposed algorithm, examining its value and limitations, as well as potential solutions. In road structures, thin layers typically appear in the shallow pavement and lack suitable targets. In this case, FWI proves advantageous for thin-layer inversion and provides prior conditions for the BP algorithm in deeper layers. As analyzed in the simulation experiments, the BP algorithm's time delay estimation propagates errors as the number of layers increases when thin layers are present. Therefore, in this dataset, two thin asphalt layers were merged into a single layer for the BP algorithm to reconstruct the targets, while the layer interface reconstruction still considered them as two separate structures. The comparison between the real data and corresponding simulations further demonstrated the effectiveness of this synergistic approach.

This article highlights both the strengths and limitations of the proposed algorithm in practical scenarios. The synergy between the BP algorithm and FWI enhances the robustness and accuracy of layered environment reconstructions, especially in managing complex subsurface features. However, challenges remain, particularly in accurately reconstructing thin layers without suitable point targets. Future research will focus on refining the algorithm's capability to differentiate and accurately reconstruct such thin layers independently, possibly by integrating additional data processing techniques or enhancing current correction methods. These improvements could significantly broaden the algorithm's applicability and accuracy in real-world engineering contexts, making it a valuable tool for infrastructure assessment and maintenance.

Acknowledgment

The authors would like to thank Audrey Van der Wielen, and Colette Grégoire from the Belgian Road Research Centre (BRRC), Wavre, Belgium.

References

[1] P. Li, H. Wang, Y. Wang, and Q. Wu, "Analysis of GPR high-frequency electromagnetic wave propagation characteristic in dispersive media," *Prog. Geophys.*, vol. 38, no. 5, pp. 2276–2287, 2023.

[2] A. Alzarrad, C. Wise, A. Chattopadhyay, S. Chowdhury, A. Cisko, and J. Beasley, "Railroad infrastructure management: A novel tool for automatic interpretation of GPR imaging to minimize human intervention in railroad inspection," *CivilEng*, vol. 5, no. 2, pp. 378–394, Apr. 2024.

[3] A. Elseicy, A. Alonso-Díaz, M. Solla, M. Rasol, and S. Santos-Assunçao, "Combined use of GPR and other NDTs for road pavement assessment: An overview," *Remote Sens.*, vol. 14, no. 17, p. 4336, Sep. 2022.

[4] X. Zhou, H. Chen, and T. Hao, "Efficient detection of buried plastic pipes by combining GPR and electric field methods," *IEEE Trans. Geosci. Remote Sens.*, vol. 57, no. 6, pp. 3967–3979, Jun. 2019.

[5] F. Tosti and C. Ferrante, "Using ground penetrating radar methods to investigate reinforced concrete structures," *Surveys Geophys.*, vol. 41, no. 3, pp. 485–530, May 2020.

[6] T. X. H. Luo, W. W. L. Lai, and A. Giannopoulos, "Forward modelling on GPR responses of subsurface air voids," *Tunnelling Underground Space Technol.*, vol. 103, Sep. 2020, Art. no. 103521.

[7] F. Tosti and E. Slob, "Determination, by using GPR, of the volumetric water content in structures, substructures, foundations and soil," in *Civil Engineering Applications of Ground Penetrating Radar*. Cham, Switzerland: Springer, 2015, pp. 163–194.

[8] H. Liu, J. Chen, X. Zhang, D. Dai, J. Cui, and B. F. Spencer, "Collaborative imaging of subsurface cavities using ground-pipeline penetrating radar," *IEEE Geosci. Remote Sens. Lett.*, vol. 21, 2024, Art. no. 3002205.

[9] R. Persico, I. Catapano, G. Esposito, G. Morelli, G. De Martino, and L. Capozzoli, "GPR mapping of cavities in complex scenarios with a combined time–depth conversion," *Sensors*, vol. 24, no. 10, p. 3238, May 2024.

[10] A. A. Baghbadorani, S. Holbrook, E. R. Martin, N. S. Ripepi, and B. Libbey, "Radar imaging applications for mining and landmine detection," Doctoral dissertation, Dept. Geosci., Virginia Polytech. Inst. State Univ., Blacksburg, VA, USA, 2022.

[11] E. Baysal, D. D. Kosloff, and J. W. C. Sherwood, "Reverse time migration," *Geophysics*, vol. 48, pp. 1514–1524, Nov. 1983.

[12] C. Özdemir, Ş. Demirci, E. Yiğit, and B. Yilmaz, "A review on migration methods in B-scan ground penetrating radar imaging," *Math. Problems Eng.*, vol. 2014, no. 1, pp. 1–16, 2014.

[13] C. Jonason, "Automatic velocity estimation in GPR data and migration," Umeå Univ., Umeå, Sweden, Tech. Rep. urn:nbn:se:umu:diva-172024, 2020.

[14] W. W. Weibull and B. Arntsen, "Automatic velocity analysis with reverse-time migration," *Geophysics*, vol. 78, no. 4, pp. S179–S192, Jul. 2013.

[15] T. V. Nguyen, C. A. V. Le, V. T. Nguyen, T. H. Dang, T. M. Vo, and L. N. N. Vo, "Energy analysis in semiautomatic and automatic velocity estimation for ground penetrating radar data in urban areas: Case study in Ho Chi Minh city, Vietnam," in *Proc. Adv. Appl. Geospatial Technol. Earth Resources*. Cham, Switzerland: Springer, 2018, pp. 34–51.

[16] W. Lv and J. Zhang, "High-resolution permittivity estimation of ground penetrating radar data by migration with isolated hyperbolic diffractions and local focusing analyses," *Frontiers Astron. Space Sci.*, vol. 10, Jun. 2023, Art. no. 1188232.

[17] H. Jung, W. Kang, and K. Kim, "Multilayer Stolt migration algorithm for subsurface target imaging in oblique layers," *IEEE J. Sel. Topics Appl. Earth Observ. Remote Sens.*, vol. 10, no. 10, pp. 4295–4303, Oct. 2017.

[18] H. Jung and K. Kim, "Autofocusing technique based on generalized multilayer Stolt migration," *IEEE Trans. Geosci. Remote Sens.*, vol. 56, no. 3, pp. 1386–1393, Mar. 2018.

[19] H. Jung and K. Kim, "Comparison of generalized multilayer Stolt migration with reverse-time migration," in *Proc. Prog. Electromagn. Res. Symp. (PIERS-Toyama)*, 2018, pp. 1945–1947.

[20] Z. Xu, F. Su, and G. Xu, "Vertex extraction-guided local back-projection algorithm for velocity estimation using ground penetrating radar data," *Int. J. Remote Sens.*, vol. 43, no. 13, pp. 4853–4871, Jul. 2022.

[21] X. Xie, J. Zhai, and B. Zhou, "Back-fill grouting quality evaluation of the shield tunnel using ground penetrating radar with Bi-frequency back projection method," *Autom. Construct.*, vol. 121, Jan. 2021, Art. no. 103435.

[22] L. Zhou, C. Huang, and Y. Su, "A fast back-projection algorithm based on cross correlation for GPR imaging," *IEEE Geosci. Remote Sens. Lett.*, vol. 9, no. 2, pp. 228–232, Mar. 2012.

[23] Z. Liu, S. Wang, X. Gu, D. Wang, Q. Dong, and B. Cui, "Intelligent assessment of pavement structural conditions: A novel FeMViT classification network for GPR images," *IEEE Trans. Intell. Transp. Syst.*, vol. 25, no. 10, pp. 13511–13523, Oct. 2024.

[24] A. De Coster and S. Lambot, "Full-wave removal of internal antenna effects and antenna–medium interactions for improved ground-penetrating radar imaging," *IEEE Trans. Geosci. Remote Sens.*, vol. 57, no. 1, pp. 93–103, Jan. 2019.

[25] S. Lambot, E. C. Slob, I. van den Bosch, B. Stockbroeckx, and M. Vanclooster, "Modeling of ground-penetrating radar for accurate characterization of subsurface electric properties," *IEEE Trans. Geosci. Remote Sens.*, vol. 42, no. 11, pp. 2555–2568, Nov. 2004.

[26] M. Henrion et al., "Mapping and monitoring peatlands in the Belgian Hautes Fagnes: Insights from ground-penetrating radar and electromagnetic induction characterization," *Geoderma Regional*, vol. 37, Jun. 2024, Art. no. e00795.

[27] L. Gao et al., "Full-wave modeling and inversion of UWB radar data for wave propagation in cylindrical objects," *Remote Sens.*, vol. 13, no. 12, p. 2370, Jun. 2021.

[28] L. Zeng, X. Zhang, X. Xie, B. Zhou, C. Xu, and S. Lambot, "Measuring annular thickness of backfill grouting behind shield tunnel lining based on GPR monitoring and data mining," *Autom. Construct.*, vol. 150, Jun. 2023, Art. no. 104811.

[29] R. K. Karnena and S. Maiti, "An efficient full wave model for investigating layered media using bi-static ground penetrating radar," *IEEE Trans. Antennas Propag.*, vol. 71, no. 5, pp. 4618–4623, May 2023.

[30] J. C. Lagarias, J. A. Reeds, M. H. Wright, and P. E. Wright, "Convergence properties of the Nelder–Mead simplex method in low dimensions," *SIAM J. Optim.*, vol. 9, no. 1, pp. 112–147, Jan. 1998.

[31] M. Zhang et al., "Review of ground penetrating radar applications for water dynamics studies in unsaturated zone," *Remote Sens.*, vol. 14, no. 23, p. 5993, Nov. 2022.

[32] S. Lambot, L. Weihermüller, J. A. Huisman, H. Vereecken, M. Vanclooster, and E. C. Slob, "Analysis of air-launched ground-penetrating radar techniques to measure the soil surface water content," *Water Resour. Res.*, vol. 42, 2006, Art. no. W11403, doi: 10.1029/2006WR005097.

[33] K. Wu et al., "A new drone-borne GPR for soil moisture mapping," *Remote Sens. Environ.*, vol. 235, Dec. 2019, Art. no. 111456.

[34] Y. Liu et al., "Full waveform inversion of multi-frequency GPR data using a multiscale approach based on deep learning," *IEEE Trans. Geosci. Remote Sens.*, vol. 62, 2024, Art. no. 5910212.

[35] J. D. Rhoades and D. L. Corwin, "Determining soil electrical conductivity-depth relations using an inductive electromagnetic soil conductivity meter," *Soil Sci. Soc. Amer. J.*, vol. 45, no. 2, pp. 255–260, Mar. 1981.

[36] C. Warren, A. Giannopoulos, and I. Giannakis, "GprMax: Open source software to simulate electromagnetic wave propagation for ground penetrating radar," *Comput. Phys. Commun.*, vol. 209, pp. 163–170, Dec. 2016.

[37] E. M. Johansson and J. E. Mast, "Three-dimensional ground-penetrating radar imaging using synthetic aperture time-domain focusing," *Proc. SPIE*, vol. 2275, pp. 205–214, Sep. 1994.

[38] S. Lambot and F. André, "Full-wave modeling of near-field radar data for planar layered media reconstruction," *IEEE Trans. Geosci. Remote Sens.*, vol. 52, no. 5, pp. 2295–2303, May 2014.

[39] K. Wu and S. Lambot, "Analysis of low-frequency drone-borne GPR for root-zone soil electrical conductivity characterization," *IEEE Trans. Geosci. Remote Sens.*, vol. 60, 2022, Art. no. 2006213.

[40] W. Huyer and A. Neumaier, "Global optimization by multilevel coordinate search," *J. Global Optim.*, vol. 14, pp. 331–355, Jun. 1999.

[41] A. De Coster, A. P. Tran, and S. Lambot, "Fundamental analyses on layered media reconstruction using GPR and full-wave inversion in near-field conditions," *IEEE Trans. Geosci. Remote Sens.*, vol. 54, no. 9, pp. 5143–5158, Sep. 2016.

[42] F. Guangyou and M. Pipan, "Synthetic and field examples of ground-penetrating radar (GPR) profile improvement using two-phase detection techniques," *Geophysics*, vol. 68, no. 2, pp. 554–558, Mar. 2003.

[43] D. Batrakov, A. Batrakova, and M. Antyufeyeva, "Combined GPR data analysis technique for diagnostics of structures with thin near-surface layers," *Diagnostyka*, vol. 19, no. 3, pp. 11–20, 2018.

[44] L. Mertens, R. Persico, L. Matera, and S. Lambot, "Automated detection of reflection hyperbolas in complex GPR images with no a priori knowledge on the medium," *IEEE Trans. Geosci. Remote Sens.*, vol. 54, no. 1, pp. 580–596, Jan. 2016.

[45] M. Rasol et al., "GPR monitoring for road transport infrastructure: A systematic review and machine learning insights," *Construct. Building Mater.*, vol. 324, Mar. 2022, Art. no. 126686.

[46] M. Garcia-Fernandez, G. Alvarez-Narciandi, and O. Yurduseven, "GPR imaging relying on frequency-diverse compressive antennas," in *Proc. 18th Eur. Conf. Antennas Propag. (EuCAP)*, Mar. 2024, pp. 1–5.

[47] J.-Y. Rhee, K.-T. Park, J.-W. Cho, and S.-Y. Lee, "A study of the application and the limitations of GPR investigation on underground survey of the Korean expressways," *Remote Sens.*, vol. 13, no. 9, p. 1805, May 2021.

[48] A. P. Tran, F. André, C. Craeye, and S. Lambot, "Near-field or far-field full-wave ground penetrating radar modeling as a function of the antenna height above a planar layered medium," *Prog. Electromagn. Res.*, vol. 141, pp. 415–430, 2013.

[49] C. Grégoire, A. Van der Wielen, and C. Van Geem, "Determination of velocities with radar in road layers," in *Proc. 8th Int. Workshop Adv. Ground Penetrating Radar (IWAGPR)*, Jul. 2015, pp. 1–4.

Zihan Xu is currently pursuing the Ph.D. degree with Harbin Institute of Technology, Harbin, China.

She is also engaged in academic exchange at the Université catholique de Louvain, Louvain-la-Neuve, Belgium. Her research is centered on improving the accuracy and efficiency of ground-penetrating radar (GPR) in complex environments. This involves optimizing signal processing algorithms, integrating advanced machine learning techniques, and developing efficient inversion methods. Her work contributes novel approaches and technological advancements for subsurface target detection and identification. Her primary research interests include signal processing and inversion algorithms for GPR, with a focus on both traditional methodologies and deep learning-based solutions.

Hongxu Li received the B.S. degree from Harbin Institute of Technology, Harbin, China, in 2019, where he is currently pursuing the Ph.D. degree with the School of Electronics and Information Engineering.

His research interests focus on radar signal processing and inverse synthetic aperture radar (ISAR) imaging.

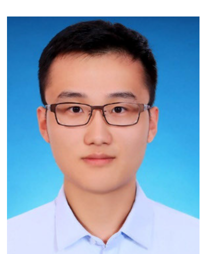

Xinfei Jin received the B.Eng. and M.Eng. degrees from Harbin Institute of Technology, Harbin, China, in 2017 and 2019, respectively, where he is currently pursuing the Ph.D. degree with the School of Electronics and Information Engineering.

His research interests include inverse synthetic aperture radar (ISAR), radar automatic target recognition (ATR), and multimodal zero-shot learning.

Fulin Su received the B.S., M.S., and Ph.D. degrees from Harbin Institute of Technology, Harbin, China, in 1986, 1989, and 2009, respectively.

Since 1989, he has been a Faculty Member with Harbin Institute of Technology, where he is currently a Professor with the School of Electronics and Information Engineering. His research interests include synthetic aperture radar (SAR) and inverse SAR (ISAR) imaging, radar signal processing, and automatic target recognition.

Dr. Su also serves as a Peer Reviewer for several international journals, such as IEEE TRANSACTIONS ON GEOSCIENCE AND REMOTE SENSING and IEEE TRANSACTIONS ON IMAGE PROCESSING.

Guodong Xu currently serves as a Professor with the School of Electronics and Information Engineering, Harbin Institute of Technology. He is also the Deputy Director of the Institute of Satellite Technology, the Chief Designer of the "Exploration No. 1" satellite, and the Chief Engineer of the "Fast Boat No. 1" and "Fast Boat No. 2" projects. His research interests include span signal and information processing, integrated electronic system design, and satellite technology, with a particular emphasis on satellite measurement, control, and pulsar navigation.

Mr. Xu is an active member of several prestigious committees, including the Aerospace Electronic Countermeasures Committee of the China Electronics Society.

Sébastien Lambot (Member, IEEE) received the M.Sc. and Ph.D. degrees in agricultural and environmental engineering from the Université catholique de Louvain (UCLouvain), Ottignies-Louvain-la-Neuve, Belgium, in 1999 and 2003, respectively, with his doctoral research focusing on ground-penetrating radar (GPR) full-wave modeling and inversion.

From 2006 to 2012, he held dual appointments at UCLouvain, where he was appointed as a Professor, and at Forschungszentrum Jülich, Jülich, Germany, where he served as the Research Group Leader. For over 24 years, he has been at the forefront of research in GPR, particularly in advancing full-wave modeling and inversion techniques for digital soil mapping and nondestructive testing. He is currently an Extraordinary Professor and the FNRS Research Director at the UCLouvain. He has published over 110 journal articles in these areas and has made numerous other contributions to the field. His research interests also encompass drone-GPR, remote sensing, hydrogeophysics, road inspection, and gesture recognition.

Dr. Lambot was awarded a European Marie-Curie Postdoctoral Fellowship, during which he conducted research at Delft University of Technology, Delft, The Netherlands, from 2004 to 2005, after his Ph.D. His expertise in Ground Penetrating Radar (GPR) has led to his active involvement in organizing several international conferences and workshops, including serving as the General Chair for the 3rd International Workshop on Advanced Ground Penetrating Radar in 2005 and the 15th International Conference on Ground Penetrating Radar in 2014. Most recently, he Co-Chaired IGARSS 2021. He has also served as an Editor for several special issues in *Near Surface Geophysics*, *Vadose Zone Journal*, and IEEE JOURNAL OF SELECTED TOPICS IN APPLIED EARTH OBSERVATIONS AND REMOTE SENSING (JSTARS).